Complete model of a spherical gravitational wave detector with capacitive transducers: Calibration and sensitivity optimization

Luciano Gottardi*

LION, Institute of Physics, Kamerlingh Onnes Laboratorium, Leiden University, Leiden, The Netherlands

(Received 5 November 2006; published 23 January 2007)

We report the results of a detailed numerical analysis of a real resonant spherical gravitational wave antenna operating with six resonant two-mode capacitive transducers read out by superconducting quantum interference devices (SQUID) amplifiers. We derive a set of equations to describe the electromechanical dynamics of the detector. The model takes into account the effect of all the noise sources present in each transducer chain: the thermal noise associated with the mechanical resonators, the thermal noise from the superconducting impedance matching transformer, the backaction noise, and the additive current noise of the SQUID amplifier. Asymmetries in the detector signal-to-noise ratio and bandwidth, coming from considering the transducers not as pointlike objects but as a sensor with physically defined geometry and dimension, are also investigated. We calculate the sensitivity for an ultracryogenic, 30 ton, 2 m in diameter, spherical detector with optimal and nonoptimal impedance matching of the electrical readout scheme to the mechanical modes. The results of the analysis are useful not only to optimize existing smaller mass spherical detector like MiniGrail, in Leiden, but also as a technological guideline for future massive detectors. Furthermore we calculate the antenna patterns when the sphere operates with one, three, and six transducers. The sky coverage for two detectors based in The Netherlands and Brazil and operating in coincidence is also estimated. Finally, we describe and numerically verify a calibration and filtering procedure useful for diagnostic and detection purposes in analogy with existing resonant bar detectors.

DOI: 10.1103/PhysRevD.75.022002 PACS numbers: 04.80.Nn, 02.60.Pn, 07.07.Mp, 95.55.Ym

I. INTRODUCTION

Resonant bar antennas are in continuous operation at 4.2 K with sensitivity and bandwidth never reached before [1,2]. These detectors could improve their sensitivity of 1 order of magnitude in the coming years when operating at 100 mK. The first ultracryogenic spherical gravitational wave (GW) detectors [3,4] are currently completing their engineering phase and will soon be operational with an expected sensitivity better than 10^{-21} $\mathrm{Hz}^{-1/2}$ at 3 kHz. Much interest is now directed towards the next generation of acoustic detectors, which will be large mass spheres [5] equipped with traditional resonant transducers and broad-band dual resonators [6,7]. The resonant spheres rely on available technology [1,2], a rather extensive theoretical work [8–13], and the ground-breaking experimental work performed so far on the ultracryogenic small mass sphere MiniGrail [3], and Mario Schenberg [4]. The wide-band dual detector potentially solves the problem of relative narrow bandwidth of current resonant bar and spheres, but the required technology needs to be assessed in separate experiments [7]. Here we numerically analyze the sensitivity and performance of an ultracryogenic spherical detector, equipped with capacitive, SQUID-based, resonant transducers. A general analysis of the problem of the readout system for a linear detector is given in [14,15]. Previous works [10,12,13,16–18] have provided a solution for the readout and inverse problem of a spherical detector, deriving equations of motion for the five degenerate quadrupole spheroidal modes coupled to N identical, pointlike, single-mode resonant transducers located at arbitrary points on the sphere surface. The effects of transducer asymmetries on the strain sensitivity and bandwidth were studied in [10,13] for rather generic radial, pointlike, single-mode, identical resonators. In [19] the strain sensitivity for a spherical gravitational wave detector with a three-mode inductive transducer with optimal parameters is calculated.

The present paper shows the results of a detailed numerical calculation of the performance of a spherical detector, which uses 2-mode capacitive transducers where the electrical resonant mode of a superconducting matching network can be tuned to the resonant mechanical modes. The signal current from the superconducting matching transformer is read out by sensitive SQUID amplifiers. We chose this transduction system mainly for two reasons: first, most existing bars and spherical antennas use capacitive transducers, second, the technology involved is so far the most advanced. As recently experimentally demonstrated on the currently most sensitive resonant antenna AURIGA [1], such a readout scheme enhances both the sensitivity and the bandwidth of a resonant detector when working in the tuned mode. Two-stage SQUID amplifiers coupled to a high quality factor load can reach nowadays an energy resolution only an order of magnitude higher than its quantum limit when properly cooled down to 100 mK [20]. Two-stage SQUID amplifiers operate at 4–5 K on the bar antenna AURIGA [1], and on the spherical

*Electronic address: l.gottardi@sron.nl
Current address: SRON, National Institute for Space Research, High Energy Astrophysics Division, Utrecht, The Netherlands

antenna MiniGRAIL [21], with a sensitivity of about $600\hbar$, never reached before.

We use the analysis presented here to study the detector sensitivity as a function of the SQUIDs, the superconducting matching network, and the mechanical resonators intrinsic parameters, and to define the optimal coupling between the antenna, transducer, and amplifiers. The simulations consider the effect of all the parameters involved in a real detector, including the effect of the cold-damping network used in the fluxed lock-loop (FLL) of the SQUID amplifier to stabilize the readout of high Q loads [22]. We study also the sensitivity and signal bandwidth deterioration coming from the transducer being a geometrically extended object rather than a pointlike mass. Finally we describe and numerically test a method to fully calibrate a spherical detector and to derive the optimal filter parameters from the experimental data. This method is a generalization of the one used with the resonant bar antenna AURIGA [23]. The codes generated to perform such an analysis can be used as a guideline for the development of future detectors as well as a tool to evaluate the performance of present small mass spherical detectors.

In Sec. II we give an overview of the equations necessary to describe the coupling of a gravitational wave to a sphere and of a sphere to a N mechanical resonator following the formalism introduced by Johnson and Merkowitz [16]. We complete the equation of motion for a capacitive transducer coupled to a SQUID amplifier through a superconducting matching transformer. The detector strain sensitivity, noise temperature, and signal bandwidth are derived using the generalized vector approach proposed by Stevenson [13]. This method is particularly powerful when transducers are not identical not only in their mechanical parameters, but also with respect to their noise sources. It indicates a rather simple method to handle the correlation between transducer output channels and to form statistically independent channels (the *mode channel* concept used in [16]) in the absence of symmetries. In Sec. III we describe all the noise sources acting on the sphere and the transducer chain. The results of the numerical analysis are reported in Sec. IV. First, following the description of a parameter optimization procedure, we calculate the strain sensitivity for an ultracryogenic spherical detector, 2 m in diameter, made of a copper and aluminum alloy (CuAl 6%), and equipped with one and six transducers located in the positions of the truncated icosahedral (TI) configuration proposed by Johnson and Merkowitz [16]. Second, the antenna patterns are calculated for two spherical detectors with optimal sensitivity located in the north and south hemisphere of the earth. The sky coverage is estimated for such spheres operating with one, three, and six resonators, both when working independently and in coincidence. Finally, the effect on the sensitivity is evaluated when nonidentical and nonideal transducers are employed. In Sec. V a complete calibration procedure for a spherical detector is described. First we show a way to derive experimentally the equivalent temperature of the mechanical modes of a sphere equipped with six transducers. Then we discuss a procedure to measure the detector transfer functions and to calibrate its force response. Such a method is finally tested by calculating the detector *mode channels* response with simulated gravitational wave bursts. Finally, Sec. VI summarizes the results.

II. SPHERICAL GW RESONANT DETECTORS

In this section we describe the model used to derive the sensitivity of a spherical gravitational wave antenna with N transducers coupled only to radial motion. We consider a capacitive transducer, which can be operated in a 2-mode configuration when the electrical mode is tuned to the mechanical one.

The dynamics of a sphere coupled to radial transducers and interacting with gravitational waves is described below using the *mode channels* formalism introduced by Johnson and Merkowitz [16], and matrices notation suitable to derive the signal-to-noise ratio (SNR) and the noise temperature of a multichannel system [13].

A. Coupling of a bare sphere with the gravitational field

A gravitational wave is a time-dependent deviation of the metric perturbation. In the coordinate frame of the wave, denoted here by primed coordinates and indices, with the origin at the detector center of mass and the z' axis aligned with the propagation direction of the wave, the spatial metric perturbation in the traceless and transverse (TT) gauge is given by

$$\mathbf{H}'(t) = \begin{pmatrix} h_+(t) & h_\times(t) & 0 \\ h_\times(t) & -h_+(t) & 0 \\ 0 & 0 & 0 \end{pmatrix}, \tag{1}$$

with h_+ and $h_\times$ corresponding to the two independent wave polarizations. A wave with polarization h_+ deforms a test ring into an ellipse with axes in the x and y directions. A wave with polarization $h_\times$ deforms the ring at a 45-degree angle to the x and y directions. A circularly polarized wave has $h_+ = \pm h_\times$ and rotates the deformation of a test ring in the right-handed (or left-handed) direction [24].

The dynamics of a bare resonant sphere can be described by ordinary elastic theory. A force f acting on the body will cause a displacement of the sphere mass element at its equilibrium position. The mechanics are described by the standard equations of motion of a forced oscillator. In this section we limit ourselves to review the main result. More complete treatments can be found in [8,9,11,12,16]. In particular we make use of the formalism introduced by Merkowitz [10,16].

Denoting by $\mathbf{f}(\mathbf{x}, t)$ the total force that acts on the sphere, including the gravitational wave force, at the position $\mathbf{x} = \{x, y, z\}$ and time t, one finds that the equation for each

mode amplitude is the one for a forced harmonic oscillator. After Fourier transforming, each mode amplitude can be written as

$$\mathbf{a}_{\mathbf{m}}(\omega) = \frac{3}{4\rho\pi R^3}\frac{1}{\omega_m^2 - \omega^2 + j\omega_m^2\Phi_m} \times \int \mathbf{\Psi}_{lm}(\mathbf{x})\mathbf{f}(\mathbf{x}, \omega)d^3x, \quad (2)$$

where R is the radius of the sphere and ρ the density. On the right-hand side of the equation, the first factor is an arbitrary normalization constant. The second factor describes the oscillating nature of the displacement where ω_m and $\Phi_m = 1/Q_m$ are, respectively, the resonance frequency and the loss angle associated with the quality factor Q_m of the mth mode. The integral is calculated over the entire volume of the sphere where $\mathbf{\Psi}_{l,m}(\mathbf{x})$ are the time-independent orthogonal elastic eigenfunctions of the sphere with $l = 0$ or $l = 2$.

In general relativity only 5 quadrupolar modes of vibration ($\ell = 2$) will strongly couple to the force density of a gravitational wave due to the fact that the tensor $\mathbf{H}'$ is traceless. In a perfect sphere they are all degenerate, having the same angular eigenfrequency ω_0. The quadrupolar modes can be written in terms of the convenient set of the five real spherical harmonics $Y_m(\theta, \phi)$, which are defined as follows:

$$\begin{pmatrix} Y_1 \\ Y_2 \\ Y_3 \\ Y_4 \\ Y_5 \end{pmatrix} = \sqrt{\frac{15}{16\pi}}\begin{pmatrix} \cos2\phi\sin^2\theta \\ \sin2\phi\sin^2\theta \\ \sin\phi\,\sin2\theta \\ \cos\phi\,\sin2\theta \\ \frac{1}{\sqrt{3}}(3\cos^2\theta - 1) \end{pmatrix}. \quad (3)$$

They are the result of a linear combination of the usual complex-valued spherical harmonics Y_{2m}.

For a sphere of radius R the eigenfunctions can be written as:

$$\mathbf{\Psi}_m = [\alpha(r)\hat{\mathbf{r}} + \beta(r)R\nabla]Y_m(\theta, \phi). \quad (4)$$

The radial eigenfunctions $\alpha(r)$ and $\beta(r)$ determine the motion in the radial and tangential directions, respectively. An explicit description of the motion in the radial and tangential directions is given by Ashby and Dreitlein [8].

In the lab frame with origin at the center of mass of the detector and the z axis aligned with the local vertical, a gravitational wave produces an effective time-dependent *tidal* force $\mathbf{F}^{\mathbf{S}}_{\mathbf{m}}$ on each mode m of the sphere equal to the overlap integral of Eq. (2). One finds

$$F_m^S(t) = \sqrt{\frac{4\pi}{15}}\rho\ddot{h}_m(t)R^4[cJ_2(qR) + 3dJ_2(kR)] = \frac{1}{2}\ddot{h}_m(t)m_S\chi R, \quad (5)$$

where J_2 is the spherical Bessel function of order 2, the coefficients c, d specify the shape of the eigenfunctions and are weakly dependent on the material Poisson ratio [9], m_S is the physical mass of the sphere, and $R\chi$ is the effective length of each mode where χ depends on the Poisson ratio and is equal to 0.327 for the CuAl sphere considered in the following analysis. h_m are the *spherical amplitudes* [16], a complete and orthogonal representation of the metric perturbation. q and k are, respectively, the longitudinal and transverse wave vectors as defined in [8]. The effective force F_m^S on the corresponding mode of a sphere is therefore uniquely determined by each spherical component of the gravitational field.

The force acting on each spheroidal mode m in the lab frame can now be written in terms of the gravitational wave amplitudes

$$\mathbf{F}^{\mathbf{S}}_{\mathbf{m}} = \frac{1}{2}m_S\chi R\omega^2\mathbf{T}_{\mathbf{V}}\begin{pmatrix} h_+ \\ h_\times \end{pmatrix}, \quad (6)$$

where $\mathbf{T}_{\mathbf{V}}$, given by

$$\mathbf{T}_{\mathbf{V}} = \begin{pmatrix} \frac{1}{2}(1 + \cos^2\theta)\cos2\phi & \cos\theta\sin2\phi \\ -\frac{1}{2}(1 + \cos^2\theta)\sin2\phi & \cos\theta\cos2\phi \\ -\frac{1}{2}\sin2\theta\sin\phi & \sin\theta\cos\phi \\ \frac{1}{2}\sin2\theta\cos\phi & \sin\theta\sin\phi \\ \frac{\sqrt{3}}{2}\sin^2\theta & 0 \end{pmatrix} \times \begin{pmatrix} \cos2\psi & \sin2\psi \\ -\sin2\psi & \cos2\psi \end{pmatrix}, \quad (7)$$

is the transformation matrix, which converts the gravitational wave amplitude in the wave frame into the spherical amplitude in the lab frame. Here we used the y-convention of the Euler angles shown in Fig. 1 and the linear combination of the spherical harmonics described in Eq. (3). The angle ψ is the first Euler angle in the rotation relating the wave frame to the laboratory frame and it carries information about the GW polarization.

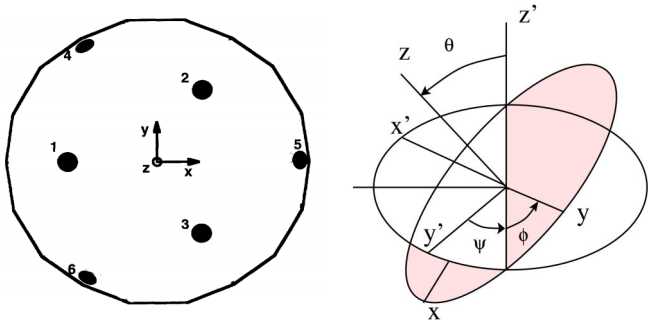

a) b)

FIG. 1 (color online). (a) The truncated icosahedral (TI) arrangement for a spherical gravitational wave antenna with resonator locations indicated. The numbering of the resonators corresponds to the ordering used in the numerical calculations. (b) Euler angle transforms convention.

B. Sphere with N resonant transducers

Resonant transducers are used on resonant detectors, either bars or spheres [1,3,25], in order to improve their sensitivity and bandwidth. We consider here the same type of transducers as displacement sensors. They consist of a mechanical resonator with the fundamental mode tuned to the quadrupolar modes of the antenna. At resonance, there is a transfer of momentum between the resonator and the antenna, turning small displacements of a large antenna into large displacements of the small resonator.

Let us consider a set of N resonators attached to the sphere at arbitrary positions (θ_j, Φ_j). The values of the relative radial displacement of the sphere at the transducers location can be grouped together into *pattern vectors* for a particular mode. These column vectors, in turn, may be put together to form a *pattern matrix* B_{mj} defined by [26],

$$B_{mj} = \frac{1}{\alpha}\mathbf{r}\cdot\mathbf{\Psi}_m(\theta_j, \phi_j), \tag{8}$$

where α is the radial eigenfunction introduced in Eq. (4). One gets

$$B_{mj} = Y_m(\theta_j, \phi_j). \tag{9}$$

Assuming that each resonator is designed to obey the one-dimensional harmonic oscillator law, the coupled equations of motion for the sphere modes, written in matrix form, are

$$\begin{bmatrix} m_S\mathbf{I} & \mathbf{0} \\ m_R\alpha\mathbf{B}^T & m_R\mathbf{I} \end{bmatrix}\begin{bmatrix} \ddot{\mathbf{a}}(t) \\ \ddot{\mathbf{q}}(t) \end{bmatrix} + \begin{bmatrix} k_S\mathbf{I} & -k_R\alpha\mathbf{B} \\ \mathbf{0} & k_R\mathbf{I} \end{bmatrix}\begin{bmatrix} \mathbf{a}(t) \\ \mathbf{q}(t) \end{bmatrix} = \begin{bmatrix} \mathbf{I} & -\alpha\mathbf{B} \\ \mathbf{0} & \mathbf{I} \end{bmatrix}\begin{bmatrix} \mathbf{F^S}(t) \\ \mathbf{F^R}(t) \end{bmatrix}, \tag{10}$$

where matrices are denoted by bold fonts and capital letters and vectors by bold fonts and lower case letters. The vector $\mathbf{a}$ has 5 components and the vector $\mathbf{q}$ has N components. They represent the radial displacement of the sphere and the resonator, respectively. For identical sphere modes and identical transducers, the factors m, k, indicating, respectively, mass and spring constants are identical and can be treated as numbers. In reality, each mode has its own mass, quality factor, and spring constant, so they have the form of a diagonal matrix with components m_i^s, $k_i^s = m_i^s\omega_i^2(1 + i\Phi_i(\omega))$ for the sphere, with $i = 1, \ldots, 5$ and m_j^r and $k_j^r = m_j^r\omega_j^2(1 + i\Phi_j(\omega))$ for the resonators, with $j = 1, \ldots, N$. Here ω_n, with $n = i, j$, is the natural frequency and $\Phi_n(\omega)$ is the loss angle of each resonant mode. It represents the frequency dependence of the loss of a mode. For commonly observed dissipations in metals [27], losses do not depend on frequency and $\Phi_n(\omega) = 1/Q_n$ where Q_n is the mode quality factor. In the case of viscous damping, due, for example, to eddy-current effects, the loss angle is proportional to the frequency and is given by $\Phi_n(\omega) = \omega/\omega_n Q_n$. We consider the first dissipation mechanism to describe the losses in the mechanical modes. $\mathbf{F^S}$ and $\mathbf{F^R}$ are the driving forces, which include the gravitational waves contribution as well as the forces generated by noise sources.

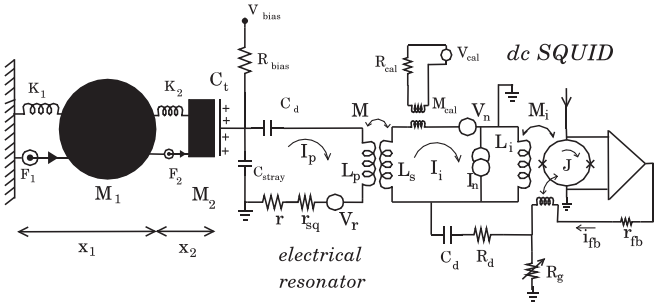

FIG. 2. Single-mode electromechanical model of a spherical antenna with mechanical resonator and capacitive transducer coupled to a SQUID through a superconducting matching transformer.

Equation (10) fully describes the mechanical system sphere-resonators when the *pattern matrix* B_{mj} is known. Here we consider the special transducer configuration proposed by Johnson and Merkowitz [16,28]. It consists of a set of six transducers placed on the 6 pentagonal faces of a TI. The resonators are located at two polar angles, $\theta_{\mathrm{TI}} = 37.3773°$ and $79.1876°$ as illustrated in Fig. 1. Their azimuthal angles ψ_{TI} are multiples of 60°.

Below we derive the complete equations of motion for a spherical detector equipped with capacitive transducer and SQUID amplifiers. In a capacitive transducer, the resonating mass, tuned to the spheroidal modes, modulates the charge of a parallel plate capacitor biased at a large constant voltage. The capacitor is formed by the resonating mass top surface and an electrode, assembled with a gap of the order of tens of micrometers. The input coil of the dc-SQUID chip is coupled to the capacitive transducer via a high-Q superconductive transformer, which can have, eventually, the electric resonance coupled to the mechanical modes in order to enhance the bandwidth. The superconducting transformer is essential to match the low impedance of the SQUID with the high impedance of the capacitor. In the model, which is schematically shown in Fig. 2, we include the relevant Gaussian noise sources of the readout scheme.

C. Equation of motion of a spherical detector with resonant capacitive transducers

The motion equations of a single capacitive transducer coupled to one mechanical mode of the sphere can be generalized to include the complete mechanical response of a sphere coupled to N resonators, described by Eq. (10), and all the equations for the electrical circuit of each resonator. After Fourier transforming, Eq. (10) can be simplified defining the following $5 + N$ square matrices:

$$\mathbf{M} = \begin{bmatrix} m_S\mathbf{I} & \mathbf{0} \\ m_R\alpha\mathbf{B}^T & m_R\mathbf{I} \end{bmatrix},$$
$$\mathbf{K} = \begin{bmatrix} k_S\mathbf{I} & -k_R\alpha\mathbf{B} \\ \mathbf{0} & k_R\mathbf{I} \end{bmatrix}, \quad (11)$$
$$\mathbf{A} = \begin{bmatrix} \mathbf{I} & -\alpha\mathbf{B} \\ \mathbf{0} & \mathbf{I} \end{bmatrix}.$$

They are, respectively, the mass, elastic, and force matrices of the coupled sphere. The force matrix $\mathbf{A}$ describes the mechanical coupling between the $5 + \mathrm{N}$ resonant modes of the detector. We can finally write

$$[-\omega^2\mathbf{M} + \mathbf{K}]\begin{bmatrix} \mathbf{a}(\omega) \\ \mathbf{q}(\omega) \end{bmatrix} = \mathbf{A}\begin{bmatrix} \mathbf{F_N^S}(\omega) \\ \mathbf{F_N^R}(\omega) \end{bmatrix}. \quad (12)$$

We assume that each of the N transducers mounted on the sphere has the same electrical circuit configuration described in Fig. 2, but not necessarily the same value of the parameters. We shall define then the vectors $\mathbf{I_p}(\omega) = (I_{p,1} \ldots I_{p,N})$, $\mathbf{I_i}(\omega) = (I_{i,1} \ldots I_{i,N})$, $\mathbf{V_r}(\omega) = (V_{r,1} \ldots V_{r,N})$, $\mathbf{V_n}(\omega) = (V_{r,1} \ldots V_{n,N})$, which describe, for each transducer, respectively, the current in the superconducting matching transformer, the current in the input coil of the dc-SQUID amplifier, the voltage noise generated in the LC superconducting resonators, and the voltage noise of the dc-SQUID amplifiers.

Denoting by E_i the electric field stored in the ith capacitive transducer, we define the electric field matrix as follows:

$$\mathbf{E} = \mathrm{diag}(E_1, \ldots, E_N). \quad (13)$$

The electrical circuit equations can be written in matrix form as follows

$$\begin{bmatrix} \mathbf{E} & \mathbf{Z_{11}} & \mathbf{Z_{12}} \\ \mathbf{0} & \mathbf{Z_{21}} & \mathbf{Z_{22}} \end{bmatrix}\begin{bmatrix} \mathbf{q}(\omega) \\ \mathbf{I_p}(\omega) \\ \mathbf{I_i}(\omega) \end{bmatrix} = \begin{bmatrix} \mathbf{I} & \mathbf{0} \\ \mathbf{0} & \mathbf{I} \end{bmatrix}\begin{bmatrix} \mathbf{V_r}(\omega) \\ \mathbf{V_n}(\omega) \end{bmatrix}. \quad (14)$$

We chose the electric matrix $\mathbf{E}$ to be diagonal, because we made the reasonable assumption that the electric field force acts only on the resonator which the field is applied to. The impedance matrix

$$\mathbf{Z} = \begin{bmatrix} \mathbf{Z_{11}} & \mathbf{Z_{12}} \\ \mathbf{Z_{21}} & \mathbf{Z_{22}} \end{bmatrix} \quad (15)$$

is a $(N + N) \times (N + N)$ matrix. Each of the four $N \times N$ matrices $\mathbf{Z_{ij}}$ is diagonal if we consider as negligible the possible crosstalk between the readout electronics of each transducer. Each diagonal member of $\mathbf{Z_{ij}}$ is equal to

$$Z_{11}^i = r^i + r_s^i + j\omega L_p^i + \frac{1}{j\omega C_p^i}, \qquad Z_{12}^i = -j\omega M^i,$$
$$Z_{21}^i = -j\omega M^i, \qquad Z_{22}^i = j\omega(L_s^i + L_{in}^i), \quad (16)$$

where r^i is a resistance associated with the losses in the superconducting resonator. C_p^i is the total transducer capacitance resulting from the parallel between the transducer and parasitic capacitance. r_s is a lossless resistance resulting from operating the SQUID amplifier in the FLL. There is no thermal noise contribution associated to r_s because it is the result of a feedback mechanism. Such a resistance can be controlled by implementing a cold-damping system [22]. In this way the detector has a virtual low quality factor making the FLL electrically stable. We remark that introducing such a damping scheme in our calculations brought benefit to the numerical analysis, by eliminating the computational problem of sharp resonances.

To fully describe the mechanical and electrical dynamics of the detector we have to introduce the backaction of the electrical readout circuit on the mechanical system. The current flowing in the LC loop of the circuit in Fig. 2 generates a force on the mechanical resonator proportional to the current itself and the applied electric field. The backaction force vector $\mathbf{F_{BA}^R}(\omega)$ adds to the Langevin force generators $\mathbf{F_N^R}(\omega)$ introduced in Eq. (12) and is equal to

$$\mathbf{F}_{\mathbf{BA}}^{\mathbf{R}}(\omega) = \left(\frac{E_1 I_{p,1}}{j\omega} \ldots \frac{E_N I_{p,N}}{j\omega}\right) = \frac{\mathbf{E}\,\mathbf{I_p}(\omega)}{j\omega}. \quad (17)$$

The complete set of coupled equations of motion becomes finally:

$$\begin{bmatrix} \mathcal{M} & \mathbf{Z_{BA}} & \mathbf{0} \\ \mathbf{0}\ \mathbf{E} & & \mathbf{Z} \\ \mathbf{0}\ \mathbf{0} & & \end{bmatrix}\begin{bmatrix} \mathbf{a}(\omega) \\ \mathbf{q}(\omega) \\ \mathbf{I_p}(\omega) \\ \mathbf{I_i}(\omega) \end{bmatrix} = \mathbf{A}'\begin{bmatrix} \mathbf{F_N^S}(\omega) \\ \mathbf{F_N^R}(\omega) \\ \mathbf{V_r}(\omega) \\ \mathbf{V_n}(\omega) \end{bmatrix}, \quad (18)$$

where $\mathcal{M} = -\omega^2\mathbf{M} + \mathbf{K}$, $\mathbf{Z_{BA}}$ is the $(5 + N) \times N$ backaction matrix given by

$$\mathbf{Z}_{\mathbf{BA}} = \begin{bmatrix} -\alpha\mathbf{B} \\ \mathbf{I} \end{bmatrix}\frac{\mathbf{E}}{j\omega}, \quad (19)$$

and

$$\mathbf{A}' = \begin{bmatrix} \mathbf{A} & \mathbf{0} \\ \mathbf{0} & \mathbf{I} \end{bmatrix}. \quad (20)$$

The $(5 + 3N)$ square matrix on the left side of Eq. (18) can be seen as the impedance matrix $\mathcal{Z}$ of the electromechanical system. Defining $\mathbf{G} = \mathcal{Z}^{-1}\mathbf{A}'$, the SQUID input current for each transducer is given by

$$\mathbf{I}_{\mathbf{i}} = \mathbf{G_I}\begin{bmatrix} \mathbf{F}_N^{\mathbf{S}}(\omega) \\ \mathbf{F_N^R}(\omega) \\ \mathbf{V_r}(\omega) \\ \mathbf{V_n}(\omega) \end{bmatrix} = \mathbf{G_I}\mathbf{F}, \quad (21)$$

where $\mathbf{G_I}$ is a submatrix of the admittance matrix $\mathbf{G}$ with components $G_{s,r}$, where $s = 5 + 2N, \ldots, 5 + 3N$ and $r = 1, \ldots, 5 + 3N$. The vectors $\mathbf{F^S}$, $\mathbf{F^R}$, $\mathbf{V_r}$, and $\mathbf{V_n}$ are the forces generated by each noise source.

The noise of the detector, referred to the SQUID amplifier input, in absence of the signal, is described by the spectral density matrix $\mathbf{S_I}$ [29]. Each component of the matrix,

$$S_I^{mn} = \int_{-\infty}^{\infty} e^{-j\omega\tau} R_{nm}(\tau) d\tau = \langle I_I^m(\omega) I_I^{n*}(\omega) \rangle, \quad (22)$$

is the Fourier transform of the correlation function for the mth and nth outputs defined as

$$R_{nm}(\tau) = \langle I_I^m(t) I_I^n(t-\tau) \rangle = \int_{-\infty}^{\infty} I_I^m(t) I_I^n(t-\tau) dt. \quad (23)$$

From Eq. (23), each component of the spectral density matrix becomes the product of the Fourier transforms of the transducer outputs, as shown in the second equality of Eq. (22). The white current noise I_0^n of the SQUID amplifier, which will be better defined below, needs to be added to the spectral matrix S_I. In matrix notation we can easily write the total SQUID current spectral density matrix as

$$\mathbf{S_I} = \mathbf{G_I F F^* G_I^*} + \mathbf{S_{I,0}}, \quad (24)$$

where the N square matrix $\mathbf{S_{I,0}}$ has components $S_{I,0}^{m,n} = I_0^m I_0^{n*}$. The diagonal elements of $S_{I,0}$ are equal to the current spectral density given in Eq. (33). The correlation between the N SQUIDs additive current noise is expected to be negligible so, in the following, we will consider diagonal the matrix $\mathbf{S_{I,0}}$. The spectral density defined in Eq. (24) can be numerically calculated and experimentally measured by means of techniques where the phase information is preserved.

The optimal signal-to-noise ratio ρ_0, for a gravitational wave signal of amplitude $\tilde{h}(\omega)$, is given by

$$\rho_0^2 = 4 \int_0^{\infty} \frac{\tilde{h}^2(\omega)}{S_{hh}(\omega)} \frac{d\omega}{2\pi}, \quad (25)$$

where

$$S_{hh}(\omega) = \mathbf{h}^*(\omega) [(\mathbf{F_m^S})^* \mathbf{G_{sig,I}^*} \mathbf{F_m^S}]^{-1} \mathbf{h}(\omega) = \frac{4}{(m_S \chi R \omega^2)^2} [\mathbf{T_V^* G_{sig,I}^*} \mathbf{S_I^{-1}}(\omega) \mathbf{G_{sig,I}} \mathbf{T_V}]^{-1} \quad (26)$$

is the one-sided total *strain* noise power spectrum.

In the equation above, we called $\mathbf{h}$ the vector $(h_+ h_\times)$ and the $N \times 5$ matrix $\mathbf{G_{sig,I}}$ is a submatrix of the admittance matrix $\mathbf{G}(\omega)$ with components $G_{s,r}$, where $s = 5 + 2N + 1, \ldots, 5 + 3N$ and $r = 1, \ldots, 5$.

Each transducer line should be considered as a linear system with the $(5 + 2N + 2)$ uncorrelated noise sources described above, if we consider as negligible the correlation between the voltage and current noise in the SQUID amplifier. However, the outputs of the N transducers do have correlated noise and the off-diagonal components of the spectral density matrix are nonzero. One can always find linear combinations of transducers outputs, which produce N uncorrelated signals [13]. Since S_I is a $N \times N$ Hermitian matrix it can be diagonalized by a unitary matrix $U(\omega)$. A new output channel vector is then obtained and is related to the original vector $\mathbf{I_i}$ by

$$\mathbf{I_i^u} = \mathbf{U^* I_i}. \quad (27)$$

The channels $\mathbf{I_i^u}$ are statistically independent and the spectral density matrix

$$\mathbf{S_i^u} = \mathbf{U^* S_i U} = \mathrm{diag}(\psi_1(\omega), \ldots, \psi_N(\omega)) \quad (28)$$

is diagonal, the eigenvalues ψ_i of $\mathbf{S_i^u}$ being the noise spectral density of each independent channel.

We notice that, after performing the diagonalization in Eq. (28), the total optimal SNR can be written as the sum of the SNR in each statistically independent output channel,

$$\rho_0^2 = \sum_{i=1}^{N} 4 \int_0^{+\infty} \frac{|I_i^{u,\mathrm{sig}}|^2}{\psi_i} \frac{d\omega}{2\pi}. \quad (29)$$

From Eqs. (25) and (26) the SNR becomes

$$\rho_0^2 = \left(\frac{m_s \chi R \omega_0^2}{2}\right) \frac{|\tilde{h}(\omega)|^2}{2\pi} \times \left[4 \int_0^{+\infty} \mathbf{T_V^* G_{sig,I}^*}(\omega) \mathbf{S_I^{-1}}(\omega) \mathbf{G_{sig,I}}(\omega) \mathbf{T_V} d\omega \right]. \quad (30)$$

The performance of resonant detectors is often characterized by their sensitivity to impulsive burst signals which vary little over the detection bandwidth. For impulsive signals, the SNR is proportional to the deposited energy E in the antenna initially at rest given by [24]

$$E = \frac{c^3}{G} \frac{1}{16\pi} \omega_0^2 |\tilde{h}(\omega_0)|^2 \Sigma = \frac{\pi}{4} \frac{\rho_S v_S^5}{f_0} \Pi |\tilde{h}(\omega)|^2, \quad (31)$$

where $\Sigma = \frac{G}{c^3} \frac{\rho v_S^5}{f_0^3} \Pi$ is the integrated cross section of a spherical detector [9] and Π is the reduced energy cross section equal to 0.215 for a CuAl sphere [12]. G and c are Newton's gravitational constant and the speed of light, respectively, while ρ_S and v_S are the antenna material density and sound velocity.

The pulse detection noise temperature T_N is then defined as

$$T_N = \frac{1}{k_B} \frac{E}{\rho_0^2}. \quad (32)$$

This is a convenient quantity to compare spherical detectors with bar detectors: while E for a bar antenna depends on source direction and polarization, T_N does not. Using Eqs. (30) and (31) we can write T_N as follows

$$T_N = \frac{4\pi}{k_B}\left(\frac{\pi}{m_S \chi R}\right)^2 \frac{\rho_S v_s^5}{\omega_0^5} \times \left[4\int_0^{+\infty} \mathbf{T_V^*} \mathbf{G_{sig,I}^*}(\omega)\mathbf{S_I^{-1}}(\omega)\mathbf{G_{sig,I}}(\omega)\mathbf{T_V} d\omega\right]^{-1}. \quad (33)$$

We remark here that, due to the dependency of the matrix $\mathbf{T_V}$ from the wave direction and polarization, the sensitivity of a spherical detector will be isotropic over the sky only if a sufficient number of transducers is used ($N > 5$). For $N < 5$, one can define the detector sensitivity by averaging over the direction and polarization as described in [30].

III. NOISE CONTRIBUTIONS

A. Mechanical resonators

Thermal noise is the main contribution of the mechanical resonators to the total detector noise. The spectral density of the thermally activated forces acting on the mechanical modes can be estimated from the fluctuation-dissipation theorem [31], and described as follows

$$\mathbf{S_{F,th}}(\omega) = 4k_B T \,\mathrm{Re}\left(\frac{\mathcal{M}}{j\omega},\right), \quad (34)$$

where $\frac{\mathcal{M}}{j\omega}$ is the system mechanical impedance matrix derived in Eq. (18), k_B is the Boltzmann constant, and T is the thermodynamic temperature. With this formalism we take into account the stochastic cross coupling among the various degrees of freedom of a macroscopic mechanical body [32].

The thermal noise contribution of other modes of the spherical detector has never been considered as a possible source of noise because they lay generally far away from the detector bandwidth. In a real detector, the first toroidal modes are only a few tens of Hz lower than the spheroidal modes due to the spread of the resonances caused by the detector asymmetry [33]. Moreover, in a spherical detector with large bandwidth, the toroidal modes shall fall into the sensitive bandwidth. However they are not sensitive to GW and they couple very weakly to a resonator with radial sensitivity. The toroidal modes usually have larger quality factors than the spheroidal modes and their thermal noise contribution is generally negligible.

Furthermore, higher frequency modes could also contribute to the total noise in the detector bandwidth due to down-conversions phenomena related to the physical geometry and dimension of the readout transducer [34]. To evaluate the contribution of the higher frequency mode one can proceed as in [35], and calculate the total mechanical impedance using finite element or numerical techniques. Here we consider only the thermal noise of the spheroidal modes and the main radial resonance of the transducers, the latter being usually the dominant source of noise. The contribution from other modes will be studied in a following paper.

B. Electrical resonators

The LC resonator which derives from transducer capacitance and the primary coil of the matching transformer contributes to the total noise with a thermal voltage noise source associated with the resonator losses, with single-sided spectral density $S_V = 4k_B T\,\mathrm{Re}(Z_{\mathrm{LC}}(\omega))$. The dissipating term $r = \mathrm{Re}(Z_{\mathrm{LC}}(\omega))$ is linked to the intrinsic electrical quality factor of the LC resonator by the well-known relation $Q_{\mathrm{el}} = \omega_{\mathrm{res}} L_p/\mathrm{Re}(Z_{\mathrm{LC}})$. The dissipation resistance r includes the contributions from dielectric losses in the transducer and decoupling capacitor, in the coil parasitic capacitance, and in the coil insulating layers and holder [36], magnetic losses due to flux motion in the superconducting shields, ''magneto-resistive'' losses due to dissipative components in the SQUID amplifier [37].

The thermal noise contribution from the LC resonator adds to the SQUID backaction noise and may become significant when SQUID amplifiers with $\epsilon < 200\hbar$ are employed.

C. SQUID amplifier noise theory

A coupled dc-SQUID amplifier can be modeled as an ideal current amplifier with a current noise source I_n in parallel and a voltage noise source V_n in series with the input coil. The two of them are responsible, respectively, for additive and backaction noise. To fully characterize the SQUID it is necessary to estimate both the noise contributions. A useful parameter to characterize an amplifier is its noise temperature T_n, defined by

$$T_n = \frac{\sqrt{S_{vv}Sii - \mathrm{Im}(S_{iv})^2}}{4k_B} = \frac{\omega}{k_B}\sqrt{\epsilon_{ii}\epsilon_{vv} - \epsilon_{iv}^2}, \quad (35)$$

in the classical limit when $k_B T_N \gg \hbar\omega$. T_n is the temperature at which the optimal input impedance gives the thermal noise power equal to the amplifier noise. Its minimum value for a linear amplifier is imposed by the uncertainty principle and is given by $T_N \sim \hbar\omega/k_B$ [38]. S_{vv} and S_{ii} are the spectral densities, referred to the SQUID input coil, of the two noise generators, while S_{vi} is the cross correlation between the two. According to the Clarke-Tesche-Giffard (CTG) theory the single-sided spectra are equal to

$$\begin{aligned} S_{ii} &\simeq 16\frac{k_B T}{R_s}\left(\frac{L_{\mathrm{SQ}}}{M_{i,\mathrm{SQ}}}\right)^2, \\ S_{vv} &\simeq 11\frac{k_B T}{R_s}\omega(M_{i,\mathrm{SQ}})^2, \\ S_{jv} &\simeq 12\frac{k_B T}{R_s} j\omega L_{\mathrm{SQ}}, \end{aligned} \quad (36)$$

where R_s, L_{SQ}, $M_{i,\mathrm{SQ}}$ are, respectively, shunt resistors, self inductance, and input coil mutual inductance of the

SQUID. The cross correlation power spectrum is always purely imaginary due to the time-reversal symmetry of the SQUID motion equation. Its absolute value is usually small and we will neglect it in the following calculations. In Eq. (35) the noise temperature is also defined in terms of the energy resolutions ϵ_{ii}, ϵ_{vv}, and ϵ_{iv} expressed in units of $\hbar$. In the following sections we will not make distinctions between the voltage and current energy resolution, ϵ_{ii} and ϵ_{vv}, and we will generically talk about SQUID energy resolution assuming that they both have the same value. The cross correlation energy resolution ϵ_{iv} will be neglected.

IV. NUMERICAL ANALYSIS

Here we numerically calculate the noise temperature, the bandwidth, and the strain sensitivity of an ultracryogenic, large 2 m in diameter, spherical detector as a function of the transduction chain parameters. We consider a detector operating according to the state-of-art resonant antenna technology and when all the parameters are improved to operate the detector nearly at the quantum limit. Further we calculate the antenna patterns and the sky coverage of two identical detectors operated in coincidence and located, respectively, in Leiden (The Netherlands) and Saõ Paulo (Brazil), the location of the two small spherical antennas MiniGrail [3], and Mario Schenberg [4], currently under development. Finally the anisotropy in the sensitivity and bandwidth is studied for a not ideal resonator and a not optimally tuned 2-mode capacitive transducer.

A. Parameters optimization

To optimize a resonant detector one must know the voltage and current noise of the available SQUID amplifier. The other parameters can then be adjusted to achieve the best SNR. The optimal impedance matching between the mechanical resonators and the SQUID amplifier is achieved when the transducer electrical mode is tuned to the mechanical resonances. In the scheme described in Fig. 2, the electrical mode contributes to the transducer chain with an equivalent mass $m_{\rm eq} = C_T E^2/\omega_{\rm el}^2$. In a multimode detector the energy transfer between each resonator is optimized when $\mu = m_R/m_{\rm eff} = m_{\rm el}/m_R$, where μ is defined as the mass ratio and $m_{\rm eff}$ is the effective mass ratio of the five spheroidal modes, which is a fraction of the sphere total mass m_s and is equal to $m_{\rm eff} = 5/6\chi m_s$ [16]. For optimal mass-ratio one gets a shorter energy transfer time between the modes and a wider system bandwidth. To fully describe the sensitivity of a resonant detector we consider the SNR, the pulse detection noise temperature T_N, and the signal bandwidth, here described by [39]:

$$\delta f = \frac{1}{2\pi} \frac{(\int_0^\infty |S_{hh}^{-2}(\omega)| d\omega)^2}{\int_0^\infty |S_{hh}^{-2}(\omega)|^2 d\omega}. \tag{37}$$

In the analysis below we imposed the following conditions:

$$E = \mu\omega_R \left(\frac{m_{\rm eff}}{C_T}\right)^{1/2}, \qquad \omega_{\rm el}^2 = \frac{1}{C_T L_r} = \omega_{\rm tr}^2, \tag{38}$$

where $L_r = L_p(1 - k^2 L_s/(L_s + L_i))$ is the reduced inductance of the primary coil of the matching transformer with coupling $k^2 = M^2/(L_s L_p)$. The first condition is obtained by assuming a constant mass ratio $\mu = m_{\rm el}/m_R$. With the second condition we impose that the electrical resonances are tuned to the transducers mechanical resonances. This condition is fundamental to get optimal matching in a capacitive transducer. The parameters of the electrical matching network depend on the value of the SQUID input inductance and noise, and on the detector mass ratio. It can be shown that for a large mass ratio, a coupling $k \sim 1$, and optimal matching, the inductance L_s of the superconducting transformer secondary coil should be as large as the SQUID input inductance L_i. However in practice large L_s will guarantee large coupling and finally a better sensitivity. For low mass ratio, the impedance seen by the transformer primary coil is lower than for high mass ratio when the same capacitance is considered. One can obtain a better matching by decreasing both the inductances L_p and L_s of the primary and secondary coil while maintaining valid the conditions equation (38). The improvement is however rather limited giving, for example, about 20% better noise temperature using an inductance $L_s \sim 0.3 L_i$ for a mass ratio $\mu = 0.001$ and a $k \sim 1$.

We anticipate that for a detector with significant thermal noise (high T/Q ratio) operating with a low noise SQUID amplifier, the optimal sensitivity is obtained for large mass ratio μ and, consequently, high transducer capacitance (see Eq. (38)). It is however physically impossible to reach arbitrary resonator high mass and capacitance using the detector configuration discussed here. The maximum transducer capacitance C_T and mass m_R one can reasonably obtain, which however have never been developed so far, are estimated to be $C_{T,\rm max} \simeq 30$ nF and $m_{R,\rm max} \simeq 90$ Kg. They correspond to a transducer with an area $A \simeq 0.1$ m^2, a gap $d \simeq 20$ μm, and a mass ratio $\mu \simeq 0.01$ [40]. We notice that strong physical constrains apply in general also to the mechanical resonant frequency due to the limits on the resonator membrane thickness [41,42]. However, a resonator ''rosette'' design as developed for the NAUTILUS and EXPLORER detectors [42], allows a rather wide freedom in the choice of the resonator mass and sensitive area for a given resonant frequency.

We report below the calculated detector sensitivity for a 2 m large in diameter, 30 ton, CuAl sphere. The main parameters of the detector are summarized in Table I. Such an antenna has a cross section $\Sigma = 9.76 \times 10^{-24}$ m^2 Hz. The total energy deposited by a GW of amplitude $\tilde{h}(\omega)$ is $E = 1.0 \times 10^{35} \omega^2 |\tilde{h}(\omega)|^2$ K. A GW burst signal, lasting for a time $\tau_G = 1$ ms, shorter than the detector integration time and rising quickly to an

TABLE I. Main parameters used in the numerical analysis of the sensitivity of a spherical detector equipped with six capacitive transducers. The first column shows the parameters of a 2 m sphere in CuAl already achieved in separate experiments. In the second column we give the parameters necessary to operate the detector at the quantum limit. The CuAl alloys have a sound velocity of 4700 m/s and a Poisson ration of about 0.3. The material dependent factor χ introduced in Eq. (5) is $\chi = 0.327$ for CuAl. The effective mass of the spheroidal modes is then $m_{\rm eff} = 5/6\chi * m_s \simeq 8$ tons.

Parameters	Current technology	Quantum limit
Sphere mass, M_s [tons]	30	30
Sphere diameter [m]	2	2
Resonator mass, M_r [Kg]	10	90
Spheroidal modes, f_l [Hz]	987, 1001, 1008, 1012, 1017	987, 1001, 1008, 1012, 1017
Q_s, Q_r, $Q_{\rm el}$	2×10^6	5×10^7
T [mK]	50	20
C_t [nF]	10	30
L_p [H]	3.6	1.2
bias field, E [Volt/m]	5×10^6	4×10^7
SQUID sensitivity, $E_{\rm res}[\hbar]$	50	1

amplitude $h_0 = \tilde{h}(\omega_0)/\tau_G \sim 2 \times 10^{-21}$, deposits an energy $T_{\rm GB} = 1\ \mu$K.

We consider a sphere equipped with six radial capacitive resonators in the TI configuration. The electrical mode of the superconducting matching network is tuned to the mechanical ones. The signal of each transducer is amplified by a two-stage SQUID amplifier. Two situations have been considered. In the first one the detector parameters have values according to the current available technology. In the second we estimate the ultimate sensitivity of the detector obtainable with quantum limited amplifiers and ultra high Q mechanical and electrical resonators. For a given T/Q ratio and SQUID amplifier energy resolution, the detector sensitivity depends on the resonators mass ratio, the electric field bias E, the transducers capacitance, and the parameters of the matching transformers.

The detector effective noise temperature, the bandwidth, and the SNR for a GW burst of $T_{\rm GB} = 10\ \mu$K are calculated as a function of the mass ratio for different values of the T/Q ratio. T/Q refers both to the mechanical and electrical resonances. The equivalent mass of the electrical resonator is adjusted according to the mass ratio by changing the electric field bias E. The optimal electrical field is calculated as a function of the mass ratio and the transducer capacitance. The results are shown in Fig. 3. We considered mechanical and electrical T/Q of 1×10^{-7}, 2.5×10^{-8}, 4×10^{-10}. Mechanical T/Q of the order of 10^{-8} has been reached in a CuAl sphere cooled at 50 mK [43], and in Al5056 bars cooled at 100 mK. The lowest $T/Q = 3 \times 10^{-8}$ for electrical resonators has been achieved by the AURIGA group with a large Nb coil resonator cooled down to 50 mK [20]. The fabrication of electrical resonators with $T/Q = 1 \times 10^{-7}$ at acoustic frequencies is nowadays a well-established technology. A $T/Q < 10^{-8}$ has not yet been achieved experimentally either in mechanical transducers or in electrical resonators. The results of the calculations are shown in plots in Fig. 4(a), where the noise temperature, the SNR, and the bandwidth are given as functions of the mass and the T/Q ratio. The SQUID amplifier coupled energy resolution was chosen to be $\epsilon_{\rm coupled} = 50\hbar$. A coupled energy resolution as low as $27\hbar$ has been recently obtained with a two-stage SQUID amplifier coupled with an electrical resonator and cooled down to $T = 50$ mK [20]. The spherical GW antenna MiniGrail and the AURIGA detector are currently operating at 5 K with SQUID amplifier energy resolution of the order of $600\hbar$ [1,21]. More than a factor of 10 improvement is expected when these detectors will operate at $T <$ 100 mK.

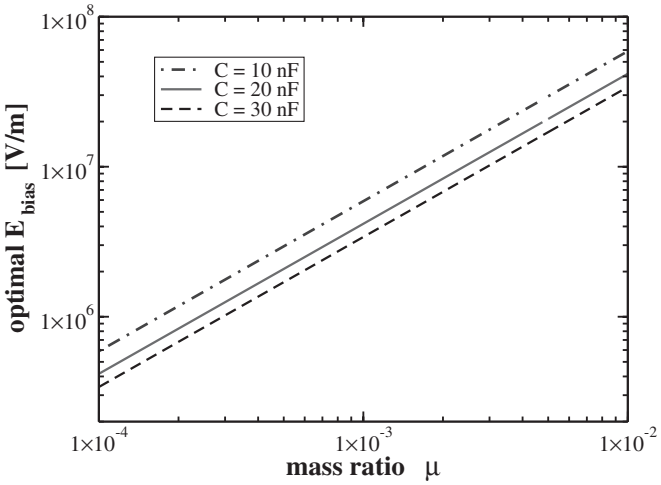

FIG. 3. Optimal bias electric field for a different value of the transducer capacitance as a function of the resonators mass ratio μ.

From the plots in Fig. 4 we see that, in terms of noise temperature and bandwidth, a large mass spherical detector developed using the available technology will not perform better than an ultracryogenic bar detector operating at the same frequency. As a matter of fact, the noise temperature T_N and the bandwidths depend only on the frequency, the electromechanical impedance matching, and the SQUID amplifier noise. However, due to the larger cross section of a spherical detector, with respect to a bar detector at the same frequency, the spherical detector improves the SNR by a factor of about 40 [12]. Moreover, omnidirectionality will of course still be a unique feature of a spherical detector when at least six resonators are used. With $T/Q = 2.5 \times 10^{-8}$ K and mass ratio $\mu = 0.001$, corresponding to a transducer resonating mass of about 9 Kg, a capacitance of 10 nF and an optimal electrical field $E = 5 \times 10^6$ V/m, the detector has a noise temperature T_N of about 10 μK, about a factor of 30 better than the present most sensitive resonant bar detector [1].

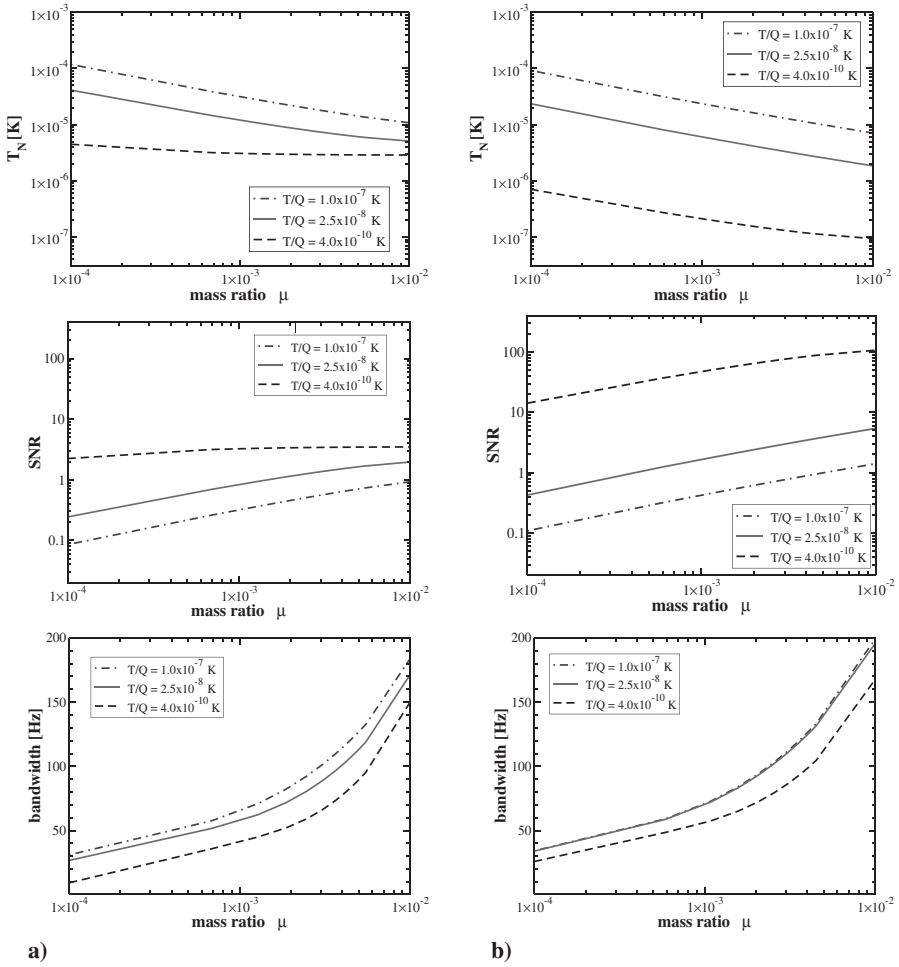

FIG. 4. Noise temperature, SNR, and bandwidth of the spherical detector as a function of the resonator mass ratio μ. The detector is read out by a $50\hbar$ energy resolution (a) and quantum limited (b) SQUID amplifier. Three different configurations with $T/Q = 1 \times 10^{-7}$ K, 2.5×10^{-8} K, and 4×10^{-10} K are studied. The SNR is calculated for a $T_{\mathrm{GB}} = 10$ μK gravitational wave burst.

The SQUID amplifier is considered strongly coupled to the electrical matching circuit assuming $k = 0.8$, $L_p \sim 1$ H, and $L_s \sim L_i = 1.7$ μH. As in bar detectors, the sensitivity will be mainly limited by thermal noise of the electrical resonator, and, outside the resonances, by the SQUID amplifier additive noise. The curves in Fig. 4(a) clearly show that large mass ratio brings benefits only to the bandwidth and not to the detector noise temperature. This is due to the fact that a large mass resonator will not help to decrease the thermal noise contribution. As a matter of fact, the contribution of the mass at the denominator of the Langevian forces derived in Eq. (34) is almost cancelled by the transfer function when transforming the forces into displacement. On the other end, the bandwidth will increase for large mass ratio due to a better impedance matching. The latter will unavoidably enlarge the contribution of the backaction noise coming from the SQUID amplifier producing the observed saturation in the detector sensitivity at large mass ratio.

To fully exploit the potentiality of a massive spherical detector one needs to develop capacitive transducers with high sensitive area, massive mechanical resonators with Q-factors larger than 10^7, high Q electrical transformers, and large bias electric fields.

In Fig. 4(b) the detector sensitivity is given for the antenna and transducer chain parameters obtainable by pushing the current technology to its limits. We consider a quantum limited SQUID amplifier operating at temperature $T < 100$ mK. Again we estimate the noise temperature T_N, the bandwidth, and the SNR for a 10 μK burst for $T/Q = 1 \times 10^{-7}$ K, 2.5×10^{-8} K, 4×10^{-10} K. By comparing those plots with the ones previously discussed, it becomes clear that without an improvement of the mechanical and electrical resonators with respect to available technology, the use of a quantum limited SQUID amplifier will not benefit the detector sensitivity. By looking at the dot-dashed curves of Fig. 4, for example, corresponding to a $T/Q = 1 \times 10^{-7}$ K, one shall expect no improvement in the strain sensitivity, but only a small increase of the bandwidth due to the lower additive noise of the SQUID. A spherical detector operating at $T = 20$ mK with mechanical and electrical quality factor $Q \sim 5 \times 10^7$, a quan-

tum limited SQUID amplifier and large mass mechanical transducers, $\mu = 0.01$ and $m_R = 90$ Kg, can have a noise temperature of 1.3×10^{-7} K, corresponding to a peak strain sensitivity of 10^{-23} Hz$^{-1/2}$ at 1 kHz, and a bandwidth of about 200 Hz. This would improve by a factor 50 the sensitivity of an existing bar or small sphere antenna working at the quantum limit. The bandwidth will have only a moderate increase with respect to the present resonant bar antennae [1], merely due to the spreading of the spheroidal modes. The minimum achievable antenna noise temperature is given by the quantum-mechanical limit of a linear motion detection derived by Giffard [44] and equal to $T_{N,\min} = 2\hbar\omega/k_B[\exp(\hbar\omega/k_B T_{N,a}) - 1]$, where $T_{N,a}$ is the noise temperature of the linear amplifier. When a quantum limited amplifier is used, $T_{N,\min} = 9.5 \times 10^{-8}$ K for a kHz resonant sphere considered here.

B. Strain sensitivity

We show here the strain sensitivity calculated using Eq. (26). The strain curves are derived for each noise contribution described in Sec. III. The readout circuit was optimized as discussed above.

In Fig. 5 the strain sensitivity is calculated for a spherical detector equipped with a single transducer placed in the position 1. It was calculated for an optimally oriented source, as will be described in detail below. The detector parameters used for this simulation have already been achieved in separate experiments [1–3]. The sensitivity curves are obtained considering the detector operating at $T = 50$ mK with a $50\hbar$ SQUID amplifier and with the electrical mode coupled to the mechanical ones. The quality factors are chosen to be $Q = 3 \times 10^6$ and $Q = 2 \times 10^6$ for the mechanical and electrical modes, respectively. The mass ratio is $\mu = 0.001$, corresponding to a mechanical resonator mass $m_R \simeq 9$ Kg. The optimal electrical bias field is about $E = 5 \times 10^6$ V/m and the transducer capacitance is 10 nF.

The strain sensitivity shown in Fig. 6 was calculated for a spherical detector with six transducers in the TI arrangement. The detector and transducers parameter are the same used in the single transducer configuration described above. Differently from the single transducer configuration, the sensitivity is independent of the wave direction and polarization. In such a configuration the detector sensitivity will be limited by the thermal noise contribution from the mechanical and electrical resonators and by the backaction noise of the SQUID amplifier due to the optimal matching coming from the tuning of the electrical resonances with the mechanical ones. Outside the resonances, the sensitivity is limited by the additive current noise of the SQUID amplifier.

In Fig. 7 the strain sensitivity is shown for an optimized detector equipped with SQUID amplifiers operating at the quantum limit. The simulation considers a detector operating at $T = 20$ mK with all resonators having quality factors $Q = 5 \times 10^7$. We consider six transducers in the TI arrangement. The mass ratio is $\mu = 0.01$ and the optimal electrical bias field is $E \sim 3 \times 10^7$ V/m. We consider a transducer with a large capacitance of about $C = 30$ nF. The sensitivity is mainly limited by additive and backaction noise of the SQUID linear amplifiers, whose minimum energy resolution is imposed by quantum mechanics. Despite the low working temperature and the high Q

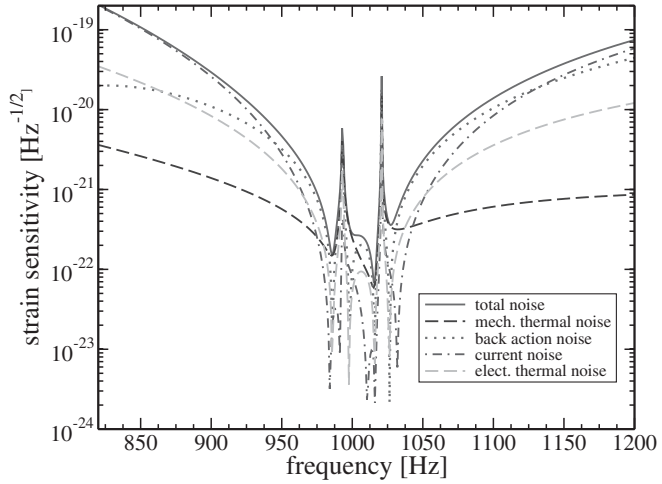

FIG. 5. Strain sensitivity for a spherical detector with one single transducer, $T/Q \sim 2.5 \times 10^{-8}$, resonators mass ratio $\mu = 0.001$, and $50\hbar$ energy resolution SQUID amplifiers. The transducer electrical mode is tuned to the mechanical ones. The parameters used for this simulation have already been achieved in separate experiments with bar detectors or a lower mass spherical antenna.

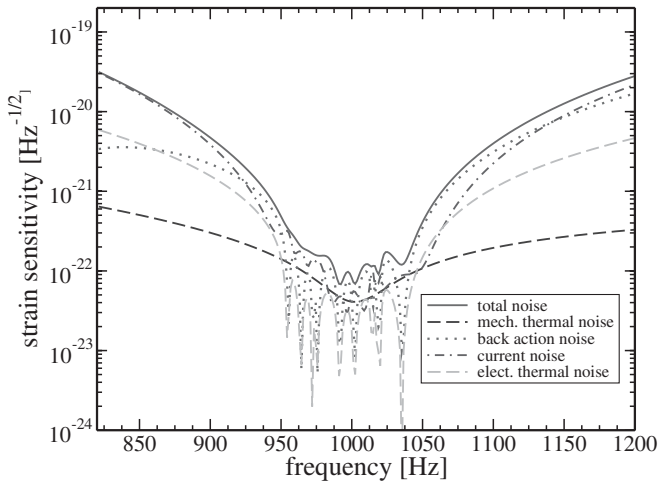

FIG. 6. Strain sensitivity for a spherical detector with six transducers, $T/Q \sim 2.5 \times 10^{-8}$, resonators mass ratio $\mu = 0.001$, and $50\hbar$ energy resolution SQUID amplifiers. The electrical modes are tuned to the mechanical ones. The parameters used for this simulation have already been achieved in separate experiments with bar detectors or a lower mass spherical antenna.

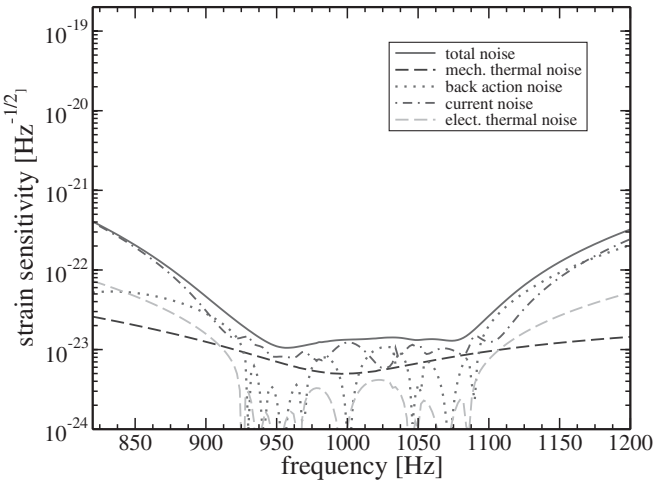

FIG. 7. Strain sensitivity for a spherical detector with $T/Q = 4 \times 10^{-10}$, resonators mass ratio $\mu = 0.01$, and $1\hbar$ energy resolution SQUID amplifiers. The electrical modes are tuned to the mechanical ones.

considered, a small contribution from the thermal noise is still present.

C. Antenna pattern

We calculate here the SNR of a spherical detector equipped with one, three, and six resonators as a function of the direction and polarization of the incident wave. We consider a detector operating at nearly the quantum limit. We numerically calculate the SNR as a function of the three Euler angles (ψ, θ, ϕ) of Eq. (7). All the three angles are necessary to completely define the GW source. The first Euler angle ψ carries information about the wave polarization [45]. The other two, (θ, ϕ), give the source direction. In the sky maps presented in this section, we call those angles, respectively, declination $\delta = \pi/2 - \theta$, and right ascension $\alpha = \phi$ to match the astronomical notation. The antenna patterns depend on the longitude and the latitude of the detector location as well as on the universal time (UT), τ, due to the earth proper rotational motion. To simplify the discussion we consider here detectors at $\tau = 0$. We calculate the antenna patterns for two spherical detectors, 2 m in diameter, located at *Leiden* (The Netherlands), lon = 4°30", lat = 52°7", and at Saõ Paulo (Brazil), lon = −46°38", lat = 23°34", where, respectively, the MiniGrail and the Mario Schenberg, 65 cm large in diameter, spherical detectors are being developed. We chose those locations because the general discussion about direction sensitivity is independent of the detector size and mass apart from the absolute value of SNR and bandwidth. The analysis presented here is then useful for the existing small spherical detectors as well.

In Fig. 8 the sky maps are shown for a spherical detector with a single transducer on position 1 of the TI arrangement. We consider a linearly polarized wave with $h_+ = h_0$ and $h_\times = 0$ and a random polarization angle ψ (sky maps at top). The amplitude h_0 is related to the deposited energy $E = k_B T_{\mathrm{GB}}$ according to Eq. (31). For each simulation we indicate the GW energy in the figure captions. The SNR for each wave direction depends on the polarization angle. The choice of a random polarization for each direction trial produces the scattered pattern. When a circularly polarized wave is chosen (sky maps at bottom) the maps become smoother and the SNR is only dependent on the wave direction. Here and in the following we consider a one-cycle, circularly polarized sinusoid: $h_+ = h_0\sqrt{2}\cos(\omega t)$ and $h_\times = h_0\sqrt{2}\sin(\omega t), 0 \le \omega t \le 2\pi$, with the frequency ω laying within the detector bandwidth. Transducers on other positions will show a similar pattern rotated on proper angles accordingly to the positions. The sky maps on the left [Fig. 8(a)] refer to a detector in Leiden with the lab frame oriented so that the z-axis is pointing to the local vertical and the x-axis to the local south. The sky maps on the right [Fig. 8(b)] refer to the detector in Saõ Paulo. As expected, in a spherical detector operating with only one transducer the sensitivity is direction and polarization dependent and changes according to the transducer location. A source emitting a linearly or circularly polarized wave is more likely to be detected when laying on the plane perpendicular to the transducer axis and passing through the sphere center.

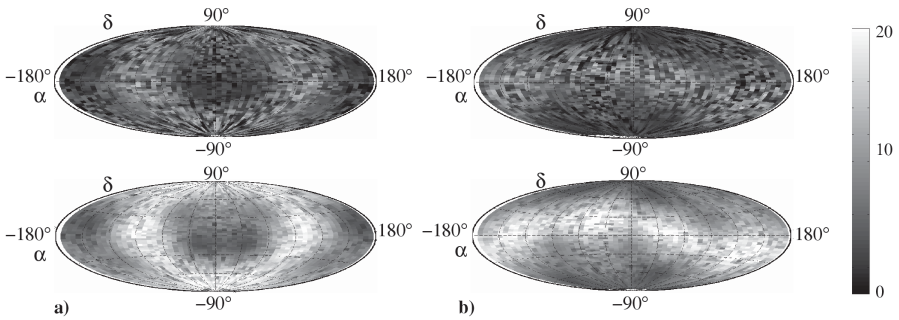

FIG. 8. Antenna pattern for spherical detectors, respectively, located in Leiden (a) and Saõ Paulo (b) with a single transducer on position 1 of the six positions of the TI arrangement. We consider a linearly polarized (top) and a one-cycle, circularly polarized (bottom) signal as explained in the text, depositing an energy $T_{\mathrm{GB}} = 3\ \mu\mathrm{K}$ in the detector.

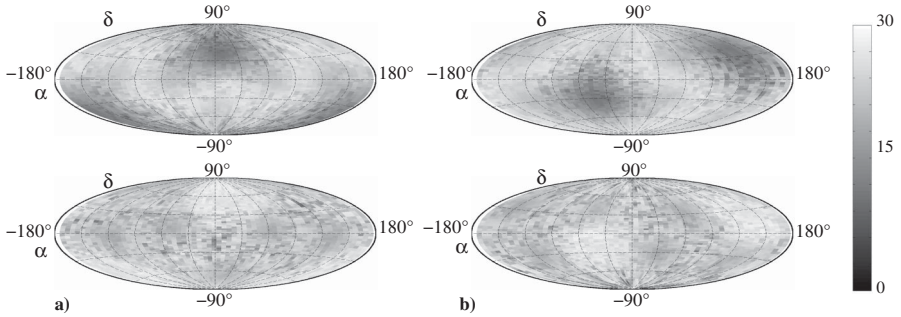

FIG. 9. Antenna pattern of spherical detectors, respectively, located in Leiden (a) and Saõ Paulo b) with a three transducers set in the TI configuration at $\theta_{\rm TI} = 37.3773°$ (sky maps above) and $\theta_{\rm TI} = 78.1876°$ (sky maps below). We consider a one-cycle, circularly polarized sinusoidal signal depositing an energy $T_{\rm GB} = 3\ \mu$K in the detector.

In Fig. 9, the sky maps are shown for a spherical detector with three transducers placed at the three positions of the TI arrangement, respectively, at $\theta_{\rm TI} = 37.3773°$ and $\theta_{\rm TI} = 78.1876°$. The signal used for the simulation is a one-cycle circularly polarized sinusoid with energy $T_{\rm GB} = 3\ \mu$K. The higher maximum SNR with respect to the single transducer configuration is mainly due to the large detector bandwidth. When six identical resonators are used, the detector becomes independent from the wave incoming direction and polarization [45]. This result is also shown in Fig. 10. For a real detector with identical transducers, not optimally tuned to the 5 spheroidal modes, a small residual anisotropy in the SNR and bandwidth is still present. This is however less than 10% over the whole sky. The signal bandwidth anisotropy is shown in Fig. 11. Both the figures will be further discussed in the following section.

Figure 12 presents the detection efficiency of a spherical detector equipped with only one transducer as a function of the GW incoming direction for different GW energies, $T_{\rm GB} = 1,\ 1.5,\ 3\ \mu$K equal to a maximum SNR, respectively, of $\rho_{\rm max} \sim 10,\ 15,\ 30$. In analogy with [46], the detection efficiency is defined as $\frac{1}{2}\mathrm{erfc}[(\eta - \rho_0)/\sqrt{2}]$, where η is a threshold chosen equal to 5 and erfc is the complementary error function. The detection of a one-cycle circularly polarized wave of energy $T_{\rm GB} = 3\ \mu$K is almost always succesful independently of the incoming direction. In Fig. 13 similar sky maps are shown for a $T_{\rm GB} = 0.6\ \mu$K when a spherical detector with 3 and 6 transducers is considered. The results of the sky maps in Fig. 12 are summarized in Fig. 14 where the fraction of sky is plotted as a function of the detection efficiency for a single transducer configuration and different signal amplitudes. One notes that the fraction of sky covered decreases when the detection probability level increases: the curves evolution for each SNR can be understood from the patterns of the sky maps in Fig. 12. The detection probability is higher than 30% in 40% of the sky for a $\rho_{\rm max} = 10$, corresponding to a 1 ms GW burst of amplitude

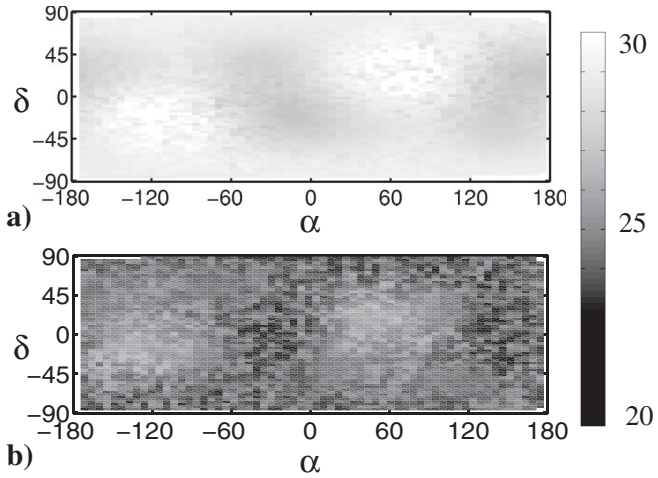

FIG. 10. SNR of a quantum limited spherical detector with six transducers in the TI configuration. In (a) identical transducers are considered. In (b) we arbitrary modified the parameters of each transducer of a maximum of 15% from their optimal value. We consider a one-cycle, circularly polarized wave with energy $T_{\rm GB} = 3\ \mu$K.

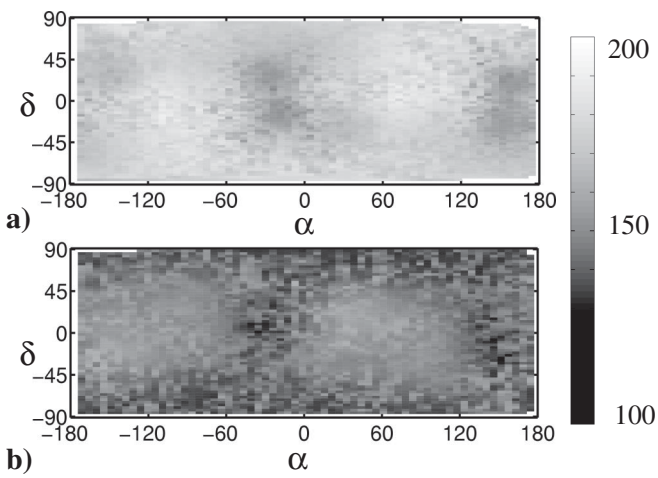

FIG. 11. Signal bandwidth of a quantum limited spherical detector with six transducers in the TI configuration. In (a) identical transducers are considered. In (b) we arbitrarily modified the parameters of each transducer of a maximum of 15% from their optimal value. We consider a one-cycle, circularly polarized sinusoidal signal with energy $T_{\rm GB} = 3\ \mu$K.

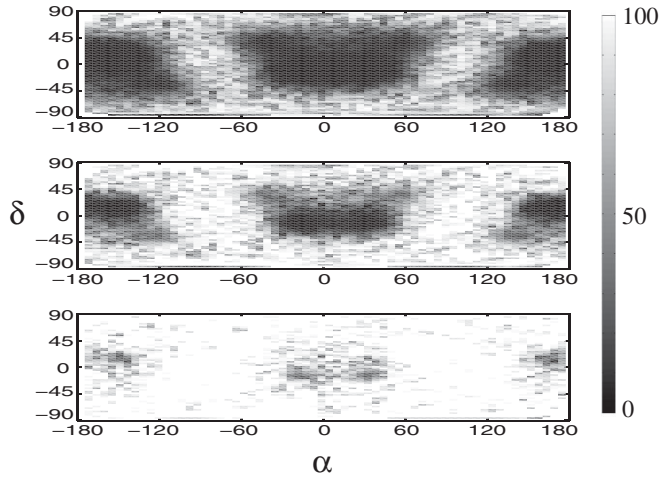

FIG. 12. Comparison of detection efficiency sky maps for a spherical detector with one transducer and for different deposited energy $T_{GB} = 1, 1.5, 3$ μK(from top to bottom). We consider a circularly polarized wave as described in the text.

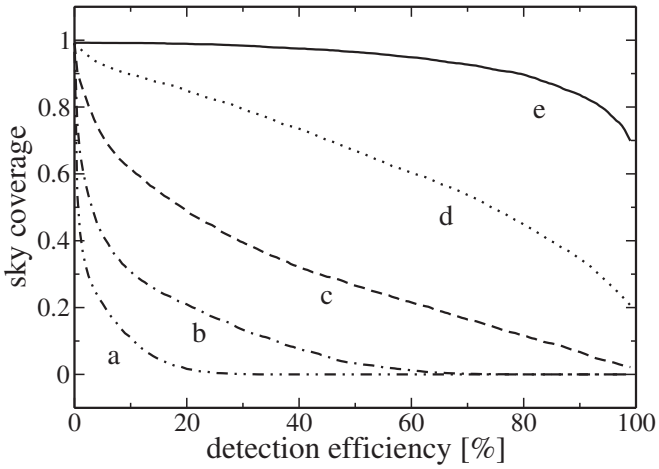

FIG. 14. Fraction of sky as a function of detection efficiency for a detector with a single transducer. We consider a circularly polarized wave with $T_{GB} = 0.6, 0.75, 1, 1.5, 3$ μK, and $\rho_{max} \sim 6, 7.5, 10, 15, 30$, respectively, denoted by **a**, **b**, **c**, **d**, and **e**.

$h_0 = 2 \times 10^{-21}$; it is 50% for almost a 70% fraction of the sky when $\rho_{max} = 15$. For $\rho_{max} \simeq 30$ the detection is likely almost in any direction.

Figure 15 presents the fraction of sky as a function of the detection efficiency of a GW burst of deposited energy $T_{GB} = 0.6$ μK for different transducer configurations. Plot (i) refers to a single spherical antenna, while plot (ii) shows the detection efficiency of two optimally oriented spherical detectors located at Leiden and Saõ Paulo. This was obtained by maximizing the portion of sky simultaneously seen by both detectors as a function of the orientation of the single detector reference system with respect to the local south. This corresponds to a rotation of the Brazilian detector lab frame (x, y, z) (see Fig. 1) around the local z-axis of about $\phi_0 = -135°$.

A detector with a single transducer is unable to detect any signal from the sky when the SNR is as low as $\rho_{max} = 6$. For the same SNR, the sky coverage of a single detector with three and six transducers is, respectively, more than

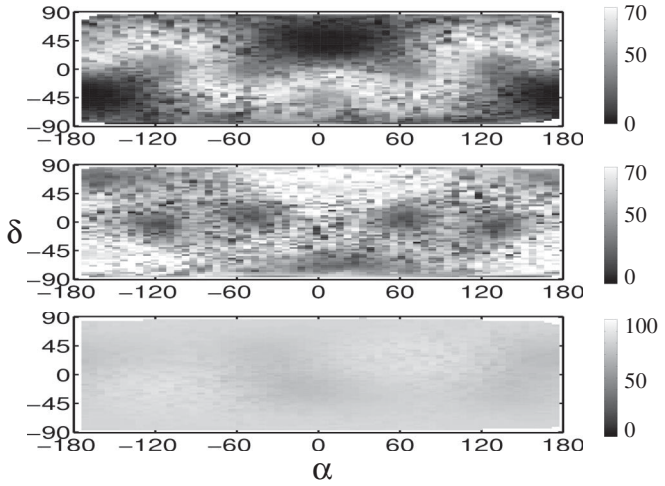

FIG. 13. Comparison of detection efficiency sky maps for a spherical detector with three transducers in the TI positions, respectively, at $\theta_{TI} = 37.3773°$ and $\theta_{TI} = 73.1876°$, and for a complete detector with 6 transducers (from top to bottom). We consider a GW burst deposited energy of 0.6 μK and a circularly polarized wave. Note the difference in the color code on the graphs and that the signal amplitude is smaller than the ones in Fig. 12.

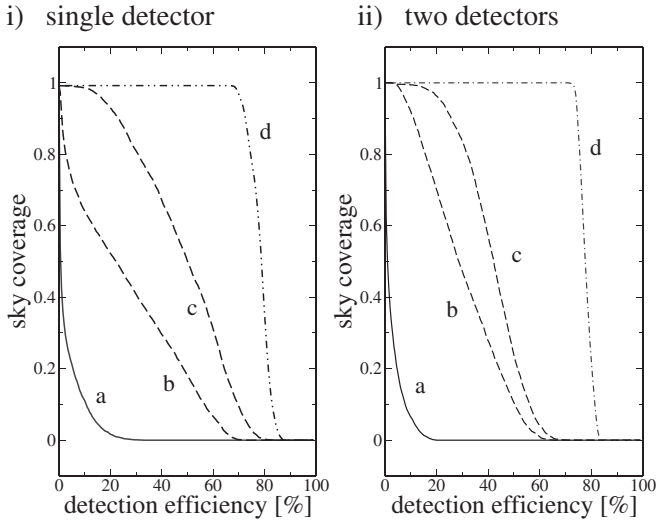

FIG. 15. Fraction of the sky as a function of the detection efficiency for a GW burst of deposited energy $T_{GB} = 0.6$ μK and $\rho_{max} = 6$ for a single spherical antenna (i) and two optimally oriented spherical detectors (ii) located at Leiden and Saõ Paulo. Curve **a** corresponds to a readout configuration with a single transducer located in position 1 of each detector, curves **b** and **c** to a three transducers configuration with $\theta_{TI} = 37.3773°$ and $\theta_{TI} = 73.1876°$, and curve **d** to a complete spherical detector with 6 transducers.

40% and 100% with 50% detection efficiency. This is mainly due to the increase of detector bandwidth when more than one transducers are used. Figure 15(b) shows that for a detector with one or three transducers, the two-fold coincidence probability remains lower than the detection efficiency of a single sphere. Two spherical antennas with six transducers can equally detect any sources in the sky even when the SNR is as low as $\rho_{\max} = 6$.

D. Sensitivity of a sphere with not ideal transducers

It has been shown that for a perfect sphere the resonators mistuning and misplacing has little effect on the isotropy when the deviation from the ideal TI configuration is less than 1% [13,45]. We study here two other possible degradation effects which may arise in a real spherical detector. The first is related to the broken spheroidal mode degeneracy and the second to the fact that a real transducer is not a pointlike mass as generally considered. In a real detector the spheroidal mode degeneracy is broken due to the suspension and the holes made on its surface to house the transducers. The modes spreading can be as large as 5% of the main resonance. It becomes natural to ask to which modes each transducer should be tuned and how good the tuning should be to avoid a sensitivity degradation. We consider here a numerical analysis of the transducer mechanical and electrical mistuning for a sphere with six resonators with a mass ratio $\mu = 0.01$ and operating at nearly the quantum limit.

In Fig. 16(a), we see the effect on the SNR for a $T_{\rm GB} = 3\ \mu$K circularly polarized GW burst when the natural resonances of each resonator are modified from the initial values $\omega_0 = 2\pi[987\ 1001\ 1001\ 1008\ 1012\ 1017]$, arbitrarily chosen equal to each of the spheroidal mode resonances. One finds a maximum change of 10% in the SNR for a resonator mistuning of about 10%. It is possible to optimize the tuning by shifting the resonator resonance frequency as much as indicated by the maximum of the SNR in Fig. 16(a). This procedure can be repeated several times. The result is shown in Fig. 16(b), where the SNR is maximum for each resonator around the new set of the resonators natural frequencies $\omega_1 = 2\pi[1047\ 971\ 980\ 970\ 960\ 1027]$. Such an optimal frequency set derives from a combination of multiple coupling, modes splitting, and transducers position. Once the bare sphere spheroidal modes and the resonator masses and positions are known, one can always find an optimal natural resonance for each resonator.

We remark here that, due to the presence of so many modes and the related multiple splitting, it could be difficult in practice to determine the resonators frequency with an accuracy better than 10% and one has probably to accept a not optimized detector. The loss in sensitivity is in any case less than 10% for a 100 Hz mistuning of the mechanical modes of a detector resonating at 1 kHz and with a tuned matching network.

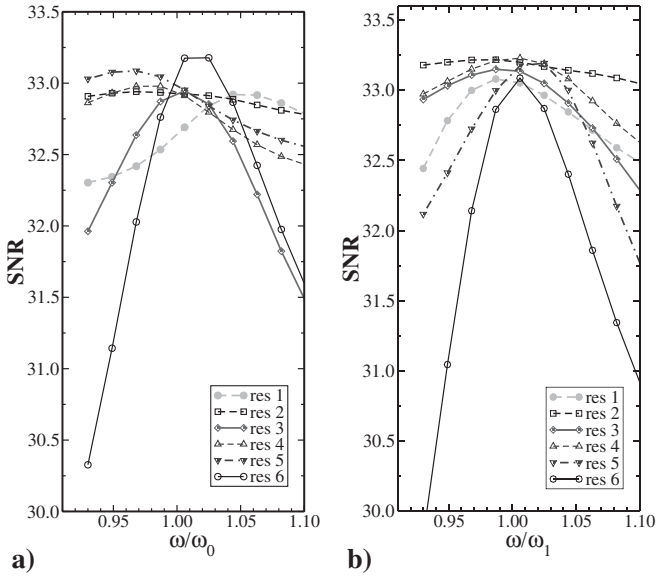

FIG. 16. Resonators mistuning. The graph shows the detector SNR for a $T_{\rm GB} = 3\ \mu$K one-cycle, circularly polarized GW burst as a function of the mistuning parameter ω/ω_0 for each resonator in the case of (a) a starting arbitrary set of natural resonances $\omega_0 = 2\pi[987\ 1001\ 1001\ 1008\ 1012\ 1017]$ and (b) an optimized set $\omega_1 = 2\pi[1047\ 971\ 980\ 970\ 960\ 1027]$ obtained after few tuning iterations.

So far we consider the transducers operating on the sphere all identical except for their main resonance frequency. Here we evaluate the effect on the detector anisotropy in the sensitivity and bandwidth, which derives from using six not identical transducers to read out the five quadrupolar mode of the sphere. We arbitrarily modified the parameters of each transducer such as the mass, mechanical, and electrical quality factor, transducer capacitance, electrical coupling factor, and SQUID noise of a maximum of 15% from their optimal value. As shown in Fig. 10(b), the detector SNR, for a circularly polarized GW burst with $T_{\rm GB} = 3\ \mu$K, is reduced about 30%. This is mainly due to a decrease in signal bandwidth as one can see from Fig. 11(b).

In the following we study how the detector sensitivity decreases when the transducer electrical resonator is not perfectly matched to the mechanical resonator. Such a situation could arise in practice when the electrical mode cannot be arbitrarily adjusted to the optimum value define by Eq. (38) as a consequence, for example, of a voltage leakage in the bias lines. One finds that, when the electrical mode of only one transducer is not tuned, even up to about 30% of the optimal frequency, very little effect is observed in the SNR and bandwidth. This is evident from the full circle data of Fig. 17, where the detector SNR and bandwidth for a $T_{\rm GB} = 3\ \mu$K circularly polarized GW burst is given as a function of the mistuning parameter $\omega/\omega_{\rm el}$, being $\omega_{\rm el}$ equal to the optimized mechanical resonator frequency set derived above. When all the electrical modes

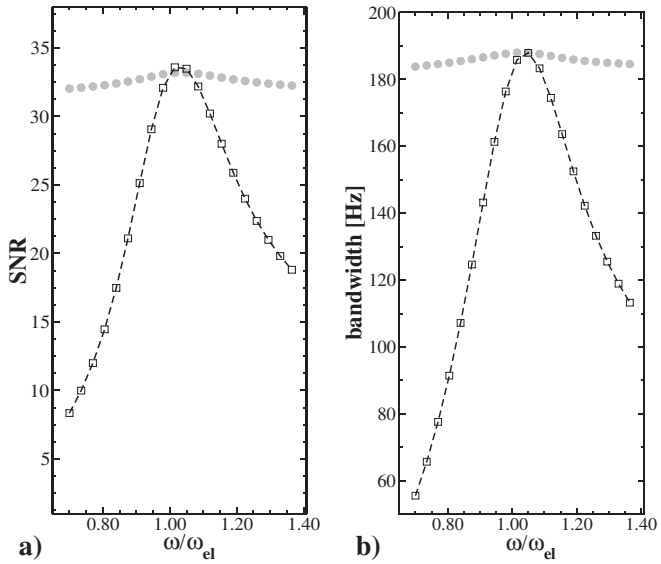

FIG. 17. Mistuning of the electrical mode. The graph shows the detector SNR (a) and bandwidth (b) for a $T_{\mathrm{GB}} = 3\ \mu$K one-cycle, circularly polarized GW burst as a function of the mistuning parameter $\omega/\omega_{\mathrm{el}}$ where ω_{el} is equal to the optimized mechanical resonator frequency set. The data show the effect when the electrical mode of only one transducer is detuned (full circles) and when the electrical modes of all the six transducers are equally mistuned (open squared).

are decoupled from the mechanical modes, the SNR and bandwidth decrease of a factor proportional to the mistuning factor as shown by the open squared data of Fig. 17.

In the numerical analysis of resonant detectors one always considers the mechanical resonators as pointlike masses. A real transducer is sampling the sphere surface radial displacement in many points belonging to the contact surface between the resonator spring and the sphere. The actual displacement can be seen as the results of an average of such a sampling. We calculated here the detector sensitivity when a real resonator is considered. Three kinds of resonators are generally used in resonant detectors: mushroom, membrane, and rosette resonators. All of them have in common the fact that the spring is attached to a support, which is rigidly connected to the antenna's surface. The variable readout considered in our calculation, in analogy with [34], can be written as

$$x(t) = \int f(\mathbf{r_t}, \mathbf{r_r}) y(\mathbf{r_t}, \mathbf{r_r}, t) dr_t dr_r, \tag{39}$$

where $y(\mathbf{r}, t)$ is the radial displacement of the intersection points between the support and the springs of the mechanical resonator used to amplify the sphere displacement. $f(\mathbf{r})$ is a form factor and the integral is calculated along the resonator support-spring intersection. We consider transducers with cylindrical symmetry where r_t is the radius of the support-spring intersection and r_r gives the radial position of the intersection points referred to the sphere center. For "mushroom," rosette, and "membrane" resonators those intersection are, respectively, the mushroom leg section, the cylindrical section where the membrane is attached to the resonator ring support, and the rosette spring sections at the attachment point with the ring support.

The form of the radial displacement depends strongly on the resonator geometry and springs topology, making it difficult to find an analytical expression like the one for the Gaussian laser beam considered in [34,35]. In the case when only the first spheroidal modes are considered, the form factor for a membrane and rosette transducer becomes

$$f_{\mathrm{memb}}(\mathbf{r_t}, \mathbf{r_r}) = \frac{s}{2\pi r_t \delta r_r} \frac{A_{12}(r_r)}{A_{12}(r_s)}, \tag{40}$$

where δr_r is the spring thickness and $A_{12}(r)$ is the spheroidal quadrupole radial amplitude function described in [11]. For a membrane transducer $s = 1$, while for a rosette transducer $s = S_{\mathrm{ros}}/S_{\mathrm{memb}} < 1$ is the ratio between the intersection surfaces defined by the rosette springs and a membrane of the same thickness.

In the case of a mushroom transducer, we have

$$f_{\mathrm{mush}} = \frac{1}{\pi r_t^2} \frac{A_{12}(r_r)}{A_{12}(r_s)}. \tag{41}$$

In proximity of the sphere surface the radial amplitude is slowly changing and the ratio $A_{12}(r_r)/A_{12}(r_s)$ can generally be approximated to 1.

In Fig. 18 the SNR and bandwidth for a circular polarized $T_{\mathrm{GB}} = 3\ \mu$K GW burst of a nearly quantum limited sphere with six resonators is shown as a function of the

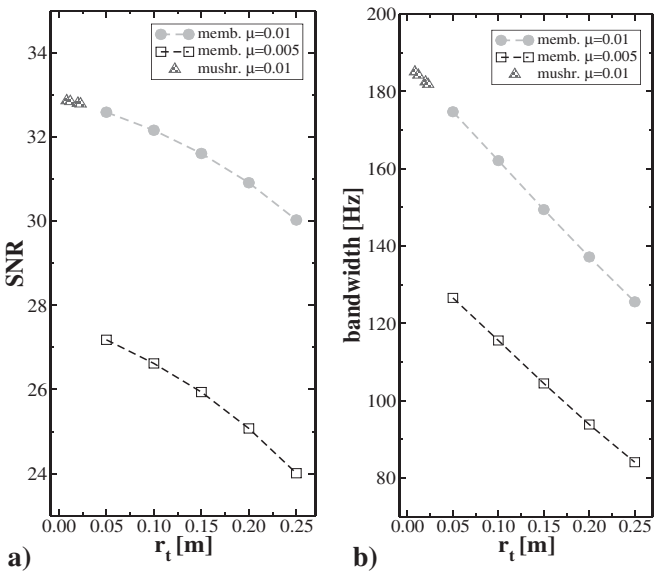

FIG. 18. Detector SNR and signal bandwidth as a function of the resonator radius r_t for a membrane resonator with mass ratio $\mu = 0.005$ (open squares), $\mu = 0.01$ (full circles), and a mushroom resonator with $\mu = 0.01$ (open triangles).

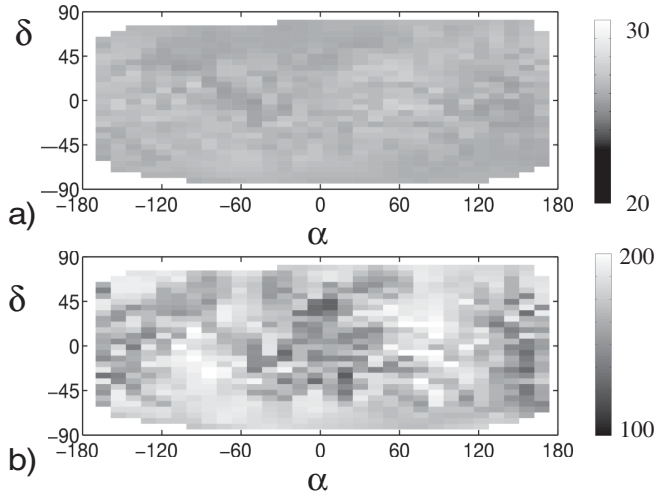

FIG. 19. Detector SNR (a) and signal bandwidth (b) anisotropy for a circular polarized GW burst with $T_{\mathrm{GB}} = 3\ \mu\mathrm{K}$ when a rosette resonator with $r_t = 0.2$ m is used to read out the sphere quadrupolar modes.

resonator radius r_t. The improvement in sensitivity, obtainable as described above by using massive resonator, with $\mu = 0.01$, is slightly reduced by the resonators large radius $r_t \sim 0.2$ m. The SNR decreases by about 10% in this case. A mushroom resonator is preferable, as shown in Fig. 18, but high Q massive resonators are difficult to achieve for such a geometry. In the sky maps shown in Fig. 19, obtained from 1000 randomly distributed events of circularly polarized GW bursts, the SNR and bandwidth anisotropy for a transducer with $r_t = 0.2$ m is shown. One finds up to 15% of asymmetry in the SNR and up to 40% in the detector bandwidth.

V. CALIBRATION OF A SPHERICAL GRAVITATIONAL WAVE DETECTOR

To calibrate a gravitational wave detector one needs to postulate a model of the complete detector whose parameters are experimentally determined. The calibration is performed in two steps. First the effective temperature of the modes is estimated. This is important in order to understand the detector dynamics and to estimate the noise contributions. Second, one has to measure the detector response to an applied force, which is equivalent to evaluating the transfer function $\mathbf{G_{sig,I}}$ in Eq. (26). We stress here that a full antenna characterization implies the estimation of the terms of the matrix $\mathbf{G_{sig,I}}$, which relates the input signal and noise to each transducer SQUID input current. It can be achieved by injecting a known signal at each step of the transducer chain, i.e. radial forces to the five spheroidal modes of the sphere, radial forces to each resonator, voltage signal in the superconducting transformer, and voltage signal at the SQUID input. In order to evaluate the sensitivity of the antenna to GW signal, however, one needs especially to measure the transfer function which converts the forces applied to the spheroidal modes to the SQUID input current of each transducer. By measuring the noise of each transducer during normal operation, one can finally estimate the strain sensitivity as in Eq. (26).

We describe below two methods that can be used to perform a complete calibration of a spherical detector in analogy with the method used for the bar detector AURIGA [1,23]

A. Modes equivalent temperature

According to the fluctuation-dissipation theorem, the voltage and current power spectra observed in an electrical circuit, when only thermal noise sources are present, are given by

$$S_V = 4\ \mathrm{kT}\,\mathrm{Re}(Z(\omega)), \qquad S_I = 4\ \mathrm{kT}\,\mathrm{Re}\left(\frac{1}{Z(\omega)}\right), \quad (42)$$

where $Z(\omega)$ is the impedance seen at the input of the amplifier used for the readout and T is the thermodynamic temperature. By measuring the transducer output spectrum in normal operation and the input impedance of the circuit one can evaluate the equivalent temperature of the transducer chain. If only thermal noise is present, the equivalent temperature of the chain should be equal to the thermodynamic temperature of the experiment. Because the SQUID is not an ideal amplifier, its current and voltage noise give a contribution to the total transducer output noise. This contribution is in general not negligible. The total current noise measured at the input of each transducer line SQUID can be written as [1]

$$S_I = 4\ \mathrm{kT}\frac{Q_a}{Q_{\mathrm{el}}}\,\mathrm{Re}\left(\frac{1}{Z(\omega)}\right) + \frac{S_{vv}(T)}{|Z(\omega)|^2} + S_{Iii}(T), \quad (43)$$

where the second term on the right-hand side of the equation is the backaction noise contribution from the SQUID amplifier with S_{vv} given by Eq. (36). Q_a is the apparent quality factor produced by the damping and Q_{el} is the intrinsic quality factor of the electrical matching network. The factor $\frac{Q_a}{Q_{\mathrm{el}}}$ in the thermal noise appears when the cold-damping network is active in the readout circuit [1]. It comes from the fact that the damping is only a lossless electronic feedback effect and there is no dissipation associated to it. From Eq. (43) we see that when the SQUID noise parameters $S_{vv}(T)$, and $S_{ii}(T)$ are known, and the impedance $Z(\omega)$ is measured, from the fit of the SQUID output current one can estimate as a fitting parameter the equivalent temperature of each transduction chain. One can measure the input impedance $Z(\omega)$ seen by the SQUID by injecting a sine-wave signal with defined level through a calibration coil weakly coupled to the SQUID input circuit.

We can simulate numerically the calibration procedure. Denoting by M_{cal} the mutual inductance between the calibration coil and the SQUID input circuit and by R_{cal} the resistance of the calibration line, to estimate the impedance

$Z(\omega)$ one has to solve the system of equations in Eq. (10). All the terms on the right-hand side are zero but the SQUID input voltage, which is given by $V_n = \frac{j\omega M_{\rm cal}}{R_{\rm cal}} V_{\rm cal}$, with $V_{\rm cal}$ the voltage of the injected calibration signal. By measuring the output response of the SQUID amplifier we obtain a direct estimation of each transducer admittance from the following weighted average:

$$\frac{1}{Z^{nn}(\omega)} = \frac{\mathrm{Re}\{I_n V_n^*\} + j\,\mathrm{Im}\{I_n V_n^*\}}{|V_n|^2} = G^{nn}_{V_n}, \qquad (44)$$

where I_n is the current at the input of each SQUID and $\mathbf{G^{nn}_V}$ was defined in Eq. (21). The weighted average gives a more precise result than simply measuring I_n/V_n. We remark that both amplitude and phase of the input and output signal have to be measured to estimate $Z(\omega)$.

The admittance $1/Z(\omega)$ can be approximated by a complex polynomial expansion with $N_p = 5 + 2 \times N$ poles and $N_q = 5 + 2 \times N - 1$ zeros as follows

$$\frac{1}{Z(\omega)} = A \frac{\Pi_{k=1}^{N_q}(j\omega - q_k)(j\omega - q_k^*)}{\Pi_{k=1}^{N_p}(j\omega - p_k)(j\omega - p_k^*)}(j\omega)^{(N_p - N_q)}. \qquad (45)$$

If ω_k and $Q_{a,k}$ are the resonant frequency and the apparent Q-factor of each measured resonance of the system, we have $p_k = j\omega_k - \omega_k/2Q_{a,k}$. The zeros q_k can be written in the same form and have frequency and Q which depends on the modes coupling. Once the admittance is measured, a polynomial fit can be performed in order to find its zero and poles.

We simulated numerically the mode temperature calibration procedure. The current noise at the input of the SQUID amplifier was estimated from Eq. (42) by calculating the impedance seen by the SQUID in the form of the admittance $1/Z(\omega)$. For simplicity we only consider two resonators located in position 1 and position 2 of the TI arrangement. The detector is at $T = 100$ mK with a $T/Q = 2.5 \times 10^{-7}$, a SQUID energy resolution of $200\hbar$ and an apparent quality factor $Q_a = 600$. The electrical modes of each transducer are tuned to the mechanical modes.

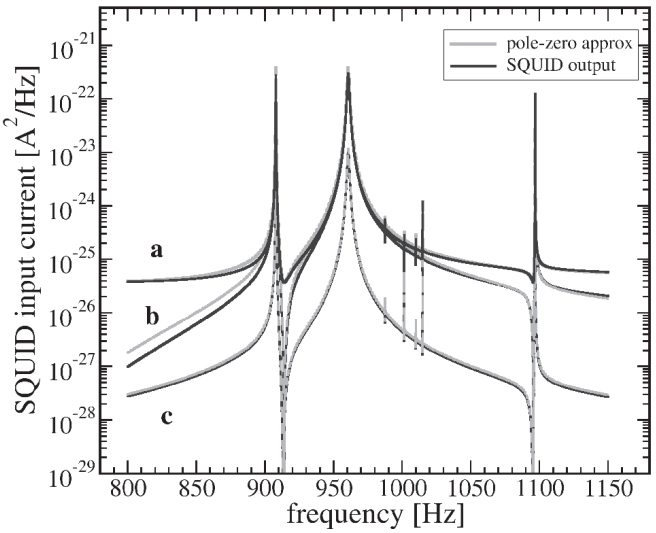

FIG. 20. Mode temperature calibration. The current noise density at the input of transducer 1 SQUID is estimated by calculation the admittance matrix $1/Z(\omega)$. The contribution from thermal noise (b), backaction noise (c), and total noise including the additive SQUID current noise (a) are shown. The gray curves are obtained from the pole-zero polynomial expansion.

Figure 20 shows the SQUID input current noise contribution from the thermal and backaction noise and SQUID additive current noise of transducer line 1. The zero-pole approximation of Eq. (45) is shown with gray curves on top of the simulated current noise contributions.

B. Force calibration and transfer functions measurements

To calibrate a spherical detector one should be able to experimentally evaluate the transfer functions which relate the output current with the GW force acting on the spheroidal modes. When a force is applied at a point (θ_c, ϕ_c) on the surface of the sphere, all the $5 + 2N$ modes of the sphere and transducers are excited at an amplitude which depends on the calibrator position, the resonators positions, and the coupling between resonators and spheroidal modes. A calibrator, consisting of a capacitive transducer with the main resonance frequency $\omega_{\rm cal}$ not tuned with the fundamental frequencies ω_0 of the detector, can be used to convert an electrical signal into a constant force acting on the sphere modes. For $\omega_{\rm cal} \gg \omega_0$, such a force is given by

$$F_c(\omega) = \frac{C_{\rm cal} E_{\rm cal}}{1 - \frac{C_{\rm cal} E_0^2}{m_{\rm cal}\omega_{\rm cal}^2}} V_{\rm cal}(\omega), \qquad (46)$$

where $C_{\rm cal}$, $E_{\rm cal}$, and $m_{\rm cal}$ are, respectively, the capacitance, the dc bias electric field, and the mass of the calibrator. $V_{\rm cal}(\omega)$ is the excitation voltage given to the calibrator at the resonance frequencies of the detector.

A force acting on the sphere surface always excites a combination of the 5 spheroidal modes. If denoted by $\mathbf{F_c} = (F_1, \ldots, F_{Nc})$ a vector of N_c radial forces applied to the N_c points $P_c = (\theta_c, \phi_c)$, with $c = 1, \ldots, N_c$, the corresponding forces $\mathbf{F_m}$ acting on the 5 spheroidal modes can be described by the calibrators pattern matrix $\mathbf{B_C}$:

$$\mathbf{F_m} = \alpha \mathbf{B_C} \mathbf{F_c}. \qquad (47)$$

From Eq. (9) we find $B_{Cm,c} = Y_{m,c}(\theta_c, \phi_c)$. The pattern matrix $\mathbf{B_C}$ has the same physical meaning as the matrix $\mathbf{B}$, but is referred to the calibrator positions. From Eq. (47) it is clear that the gravitational forces acting on each of the five quadrupole modes, distributed over the entire volume, can be simulated by a linear combination of radial forces acting on the $N_c \geqslant 5$ calibrators. This conclusion is based on the assumption that the real spherical antenna dynamics is the same as that of an ideal sphere that can fully be modeled

using the spherical harmonics approach described above. The validity of this assumption could be evaluated through a finite element analysis (FEA) of the detector structural model or by experimentally measuring the six transducers response to several linear combinations of excitations given through the calibrators.

To operate the sphere as a GW detector, only one force calibrator, mounted at an arbitrary position on the sphere surface, is necessary when $N = 6$ transducers are used in the TI configuration. This is due to the existing one-to-one relation between the *mode channels* and the forces acting on the spheroidal modes. It is convenient to proceed by transforming the N measured transducers outputs into the 5 *mode channels*, which directly describe the GW amplitude acting on the spheroidal modes [16]. In such a framework we derive the optimal filter for each mode channel to define an operative procedure to signal detection with a GW spherical resonant antenna. In order to do this we define the 5×5 mode channel noise spectral density matrix as

$$\mathbf{S}_{\mathbf{I,B}}(\omega) = \mathbf{B}\mathbf{S}_{\mathbf{I}}(\omega)\mathbf{B}^{\dagger}, \tag{48}$$

and, using the admittance matrix $\mathbf{G}_{\mathbf{sig,I}}$ introduced in Eq. (26), the 5×1 mode channel signal vector

$$\mathbf{I}_{\mathbf{g,sig}} = \mathbf{B}\mathbf{I}_{\mathbf{i}} = \alpha\mathbf{B}\mathbf{G}_{\mathbf{sig,I}}\mathbf{B}_{\mathbf{C}}\mathbf{F}_{\mathbf{c}}. \tag{49}$$

By applying a known constant force to the calibrator $\mathbf{F}_{\mathbf{c}}$, using Eq. (47) we get the linear combination of spheroidal modes forces generated by the calibration force. By measuring simultaneously the amplitude and phase of the six transducer outputs we obtain the mode channel response from Eq. (49) and, using Eq. (26), estimate the detector strain sensitivity. The matrix $\mathbf{S}_{\mathbf{I,B}}(\omega)$ in Eq. (48) is diagonal because the mode channels are statistically independent. The only assumption made here is that the pattern matrix $\mathbf{B}$ derived above for an ideal sphere can be used to describe the dynamics of the real detector with six transducer in the TI arrangement. This can be experimentally verified in a separate cryogenic experiment, using, for example, a set of six calibrators in the TI configuration with a 60° dephase of the azimuthal angle with respect to the transducer arrangement. Each spheroidal mode force can be reproduced by simultaneously applying a linear combination of constant forces on the six calibrators, as described by Eq. (47). When $N < 5$ transducers are used we cannot transform the transducer outputs in mode channels. A set of at least 5 calibrators is then necessary to experimentally measure the transducer response to each mode channel. If only one calibrator is used, the detector output can only be calibrated for a particular combination of the five quadrupolar forces F_m.

Each element on the diagonal of $S_{I,B}^{(m)} = I_m(\omega)I_m^*(\omega)$ can be written in terms of the polynomial ratio where the poles are the same as the ones derived in the impedance measurement of each transducer, see Eq. (45), and the zeros depend on the current function $I_m(\omega)$. From the factorization of $I_m(\omega)$ one finds

$$I_m(\omega) = S_{0,m}^{1/2}\Pi_{k=1}^{N_p}\frac{(j\omega - q_{k,m})(j\omega - q_{k,m}^*)}{(j\omega - p_k)(j\omega - p_k^*)}, \tag{50}$$

where $S_{0,m}$ is the wide-band noise of the mth mode channel, and equals the amplifier additive white noise if all the transducers SQUIDs are identical. From the definition in Eq. (50), $S_{I,B}^{(m)}$ is real for real ω and the number of zeros and poles is the same as a consequence of assuming S_0^m to be purely white.

The transfer functions for a GW signal, which convert the quadrupolar modes forces into mode channels currents according to Eq. (49), contain the same poles $\{p_k\}$ and their factorization becomes

$$H_m(\omega) = H_{m,\mathrm{cal}}(\omega)\frac{\Pi_{k=1}^{N_r}(j\omega - r_{k,m})(j\omega - r_{k,m}^*)}{\Pi_{k=1}^{N_p}(j\omega - p_k)(j\omega - p_k^*)}. \tag{51}$$

In the equation above $N_p > N_r$ and $H_{m,\mathrm{cal}}(\omega)$ is a force calibration constant which has to be experimentally determined at each cool down.

From now on we apply to each mode channel the standard Wiener-Kolmogorov (WK) filtering operation, developed so far for bar detectors [15]. We follow here the approach described in [23]. The best linear estimate of the amplitude h_0 of a given signal $h(t)$, with $\max h(t) = h_0$ at the arrival time $t = 0$, buried into an additive, zero mean, stationary Gaussian noise η can be obtained by correlating the mode channel output $Y_m(\omega) = \tilde{h}(\omega)H_m(\omega) + \eta(\omega)$ to the matched WK filter [39],

$$W_m(\omega) = \sigma_A^2\frac{H_m^*(\omega)\tilde{h}^*(\omega)}{S_{I,B}^{(m)}(\omega)}, \tag{52}$$

where $\sigma_A^2 = \int d\omega |H_m(\omega)\tilde{h}(\omega)|^2/S_{I,B}^{(m)}(\omega)$ is the variance of the noise after the filtering. The WK filter splits as the product $L_m(\omega)M_m(\omega)\tilde{h}^*(\omega)$, where $L_m(\omega)$ is a whitening filter for the noise $S_{I,B}^{(m)}(\omega)$ given by

$$L_m(\omega) = I_m^{-1}(\omega) = S_{0,m}^{-1/2}\Pi_{k=1}^{N_p}\frac{(j\omega - p_{k,m})(j\omega - p_{k,m}^*)}{(j\omega - q_{k,m})(j\omega - q_{k,m}^*)}. \tag{53}$$

M_m is a bandpass filter around the frequencies $\omega_k = |\mathrm{Im}(q_{k,m})|$ and bandwidths $\Delta\omega_k = 2\,\mathrm{Re}(q_{k,m})$. Such a bandwidth is generally much larger than the intrinsic bandwidth of each resonance and, in the case of a transducer with coupled electrical modes, it can reach values as large as ~200 Hz. One finds

$$M_m(\omega) = \sigma_A^2 \cdot S_{0,m}^{-1/2}\frac{\Pi_{k=1}^{N_r}(j\omega + r_{k,m})(j\omega + r_{k,m}^*)}{\Pi_{k=1}^{N_p}(j\omega + q_{k,m})(j\omega + q_{k,m}^*)}. \tag{54}$$

The product $L_m(\omega)M_m(\omega)$ is the WK filter for a deltalike

GW pulse. The extra term $\tilde{h}(\omega)$ should be added when a general GW signal $h(t)$ is considered. It can be shown that for a resonant bar detector, $N_r = 1$ and $r_1 = 0$. In this case the WK filtering procedure is then fully defined by the zeros q_k and poles p_k of the noise power spectrum $S_I(\omega)$, the additive amplifier white noise S_0, and the calibration constant $H_0(\omega)$. For a spherical detector this is true only if the quadrupolar modes degenerate into a single resonant frequency and all the transducers have the same resonance. When multiple resonances are present, as is the case for real spherical detectors, the zeros in Eq. (51) do not cancel i.e., $N_r > 1$ and $r_{k,m} \neq 0$. This is due to the fact that when the quadrupolar modes are nondegenerate, a mixing occurs between mode channels. A fraction of the signal which should only go to one mode channel leaks into the others. The WK filtering procedure should include the extra set of parameters $r_{k,m}$, whose total number depends on the mode and transducer considered and must be experimentally determined.

In Fig. 21 the mode channels response is plotted for a linearly polarized burst coming along the detector z direction. For a detector with degenerate modes, Fig. 21(a), only the second mode gives a larger signal than the noise, as can be expected for a signal from that particular direction and polarization. For a realistic detector with nondegenerate spheroidal modes a mixing between the modes is present around the resonances making the analysis more complex [see Fig. 21(b)]. However, the energy stored in the second mode, which can be derived from the integral of the SNR density, is larger than in the others and the incoming wave direction can still be reconstructed without any significant accuracy loss with respect to the degenerate case. To estimate the incoming wave direction we can use the approach derived in [12], using standard theory of signal detection. After being optimally filtered, the 5 mode channels generate a set of 5 amplitudes, g_m, for an input GW burst. The likelihood function for a detector with stationary and Gaussian noise is given by

$$\lambda = \frac{1}{2\pi} \prod_{m=1}^{5} \exp\left(-\frac{[h_m - g_m]^2}{\sigma_m^2} \right), \tag{55}$$

where h_m is the expected gravitational wave signal amplitude, g_m is the mode channels amplitude obtained after the WK filtering procedure described above, and σ_m is the variance of g_m. A likelihood map is generated by plotting this function in the declination-ascension plane, (δ, α). The maximum value of λ gives to the estimated wave direction. In the example below, a realistic detector at the quantum limit, with optimized parameter is considered. We applied simulated burst signals, 1 ms long and with amplitude $h_0 = 0.34 \times 10^{-20}$, 1.1×10^{-20}, 2×10^{-20}, and SNR $\sim$ 30, 300, 1000, with linear polarization $h_+ = h_0$ and $h_\times = 0$, coming from a source at declination $\delta = 20°$ and ascension $\alpha = 70°$. Figure 22 plots the resulting likelihood functions.

The accuracy in the direction and polarization estimates depends on the SNR and is equal to $\Delta\Omega = 2\pi/\mathrm{SNR}$ [12,13]; it is direction independent when a sphere with more than 5 identical, pointlike transducers is considered [45]. As it comes clear from the plot, a single spherical detector cannot distinguish between sources laying in the two opposite hemispheres. In the example described above

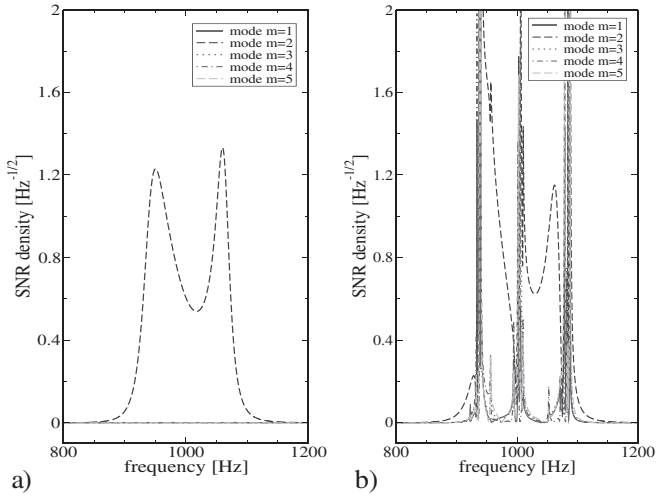

FIG. 21. Modes channels response from a simulated linearly polarized burst coming along the z direction in the detector frame for a detector with degenerate (a) and nondegenerate (b) modes. For a detector with degenerate modes (a), only the second mode gives a larger signal than the noise. For a real detector with nondegenerate modes (b), a mixing between the modes is present around the resonances making the analysis more complex.

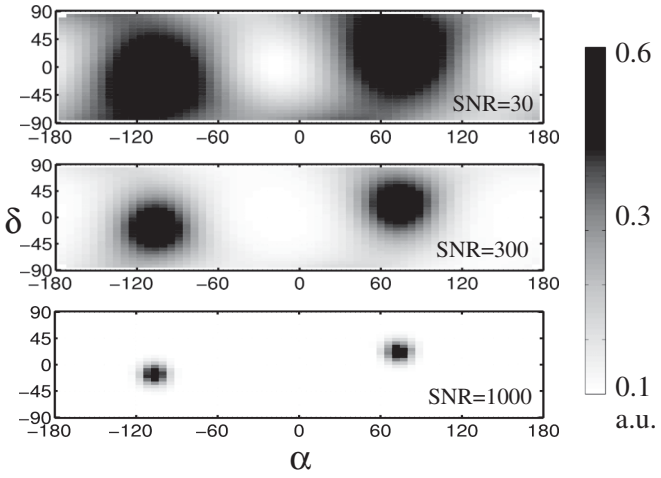

FIG. 22. Signal direction reconstruction. An overall sky search is performed calculating the likelihood function λ. We applied simulated burst signals with SNR $\sim$ 30, 300, 1000, amplitude $h_0 = 0.34 \times 10^{-20}$, 1.1×10^{-20}, 2×10^{-20}, and $\tau_{\mathrm{GB}} \sim 1$ ms, linearly polarized and coming from a source at declination $\delta = 20°$ and ascension $\alpha = 70°$. A single spherical detector cannot distinguish between sources laying in two opposite hemispheres.

we assumed for simplicity that the signal polarization was known. When this is not the case, one should include also the first Euler angle ψ as a variable to estimate the likelihood ratio.

As discussed in [13], for a known signal, the optimal detection strategy for a *vector* output detector like a sphere with N transducers is to compute the value of the optimal linear filter with *scalar* output ν which maximizes the SNR. This procedure is useful if one wants to monitor the total energy in the sphere and claim a detection only on the base of an excess of absorbed energy. No direction information is possible in this way.

If we let $\mathbf{I} = I_1, \ldots, I_N$ be the transducers output stream, a linear filtering operation is performed which, in frequency domain, can be described by

$$\nu(\omega) = \mathbf{W}^{\dagger}(\omega)\mathbf{I}(\omega), \tag{56}$$

where $\mathbf{W}$ is a vector transfer function which maximizes the SNR and was found [13] to be

$$\mathbf{W}(\omega) = \mathbf{I}^{\dagger}_{\mathbf{sig}}(\omega)\mathbf{S}^{-1}_{\mathbf{I}}(\omega). \tag{57}$$

In the above, $\mathbf{I_{sig}} = \mathbf{G_{sig}}(\omega)\mathbf{F^S_m}$ is the current generated in each transducer by a force F^S_m on the sphere generated by a GW signal. As shown in [12], the maximum SNR for a multichannel detector is the sum of the maximum SNR of each individual channel. The optimal linear filter introduced above for each mode channel is then useful in order to compute the scalar output ν which maximizes the SNR.

VI. CONCLUSIONS

We derived a complete and detailed electromechanical model for a spherical gravitational wave detector operating with multiple, two-mode capacitive transducers where the electrical resonant mode of a superconducting matching LC resonator can be tuned to the resonant modes. The signal current form the matching network is read out by SQUID amplifiers. The model allows to numerically calculate the sensitivity of a realistic detector and to study in detail the effects of the main mechanical and electrical parameters of the displacement readout system on the strain sensitivity and bandwidth. All the known noise sources are discussed and considered in the model.

A complete numerical analysis has been performed for a 2 m in diameter, 30 ton in mass, CuAl spherical detector operating at ultracryogenic temperatures. We derived the sensitivity for the spherical detector in its initial phase of development, when a single transducer is used, and when the detector operates with six transducers and becomes fully omnidirectional. The sensitivity is evaluated when the detector operates by making use of available technology and when it works at the quantum limit. We have shown that, in order to improve the strain sensitivity towards the quantum limit one should operate the detector at a temperature of about $T = 20$ mK with electrical and mechanical quality factor as high as 5×10^7 and massive mechanical resonators.

Direction anisotropies in the detector sensitivity and signal bandwidth are studied for a not ideal detector operating with not identical, partially tuned, and real-size resonators. The models made so far always consider rather generic, and pointlike transducers, neglecting the fact that those sensors are in practice rather large and spatially distributed on a significant fraction of the sphere surface. We investigated here the validity of such an assumption.

Finally we described and numerically verify a complete calibration procedure, which makes use of techniques available for bar detectors. Similar algorithms can be used on the spherical detector for diagnostic purpose and to derive the direction and polarization information from the detected signal.

ACKNOWLEDGMENTS

The author would like to thank Massimo Bassan, Florian Dubath, Jean-Pierre Zendri, and Alberto Lobo for reading this manuscript and for useful discussions. The MiniGRAIL project has been the major drive for writing this paper. This work has been financially supported by Integrated Large Infrastructures for Astroparticle Science (ILIAS) of the Sixth Framework Programme of the European Community.

[1] L. Baggio, M. Bignotto, M. Bonaldi, M. Cerdonio, L. Conti, P. Falferi, N. Liguori, A. Marin, R. Mezzena, A. Ortolan, *et al.*, Phys. Rev. Lett. **94**, 241101 (2005).
[2] P. Astone, R. Ballantini, D. Babusci, M. Bassan, P. Carelli, G. Cavallari, F. Cavanna, A. Chincarini, E. Coccia, C. Cosmelli, *et al.*, Classical Quantum Gravity **23**, S57 (2006).
[3] A. de Waard, M. Bassan, Y. Benzaim, V. Fafone, J. Flokstra, G. Frossati, L. Gottardi, C. T. Herbschleb, A. Karbalai-Sadegh, K. Kuit, *et al.*, Classical Quantum Gravity **23**, S79 (2006).
[4] O. D. Aguiar, L. A. Andrade, J. J. Barroso, F. Bortoli, L. A. Carneiro, P. J. Castro, C. A. Costa, K. M. F. Costa, J. C. N. de Araujo, A. U. de Lucena, *et al.*, Classical Quantum Gravity **23**, S239 (2006).
[5] ROG Collaboration, SFERA Project, unpublished (2005).
[6] M. Bonaldi, M. Cerdonio, L. Conti, M. Pinard, G. Prodi, and J. Zendri, Phys. Rev. D **68**, 102004 (2003).

[7] M. Bonaldi, M. Cerdonio, L. Conti, P. Falferi, P. Leaci, S. Odorizzi, G. A. Prodi, M. Saraceni, E. Serra, and J. P. Zendri, Phys. Rev. D **74**, 022003 (2006).
[8] N. Ashby and J. Dreitlein, Phys. Rev. D **12**, 336 (1975).
[9] R. V. Wagoner and H. J. Paik, in *Proceedings of the Pavia International Symposium, Pavia, Italy* (Academia Nazionale dei Lincei, Rome, Italy, 1977).
[10] S. M. Merkowitz, Phys. Rev. D **58**, 062002 (1998).
[11] J. Lobo, Phys. Rev. D **52**, 591 (1995).
[12] C. Z. Zhou and P. F. Michelson, Phys. Rev. D **51**, 2517 (1995).
[13] T. R. Stevenson, Phys. Rev. D **56**, 564 (1997).
[14] J. C. Price, Phys. Rev. D **36**, 3555 (1987).
[15] G. V. Pallottino and G. Pizzella, Nuovo Cimento Soc. Ital. Fis. C **4**, 237 (1981).
[16] S. M. Merkowitz and W. W. Johnson, Phys. Rev. D **51**, 2546 (1995).
[17] J. A. Lobo and M. A. Serrano, Europhys. Lett. **35**, 253 (1996).
[18] J. A. Lobo, Mon. Not. R. Astron. Soc. **316**, 173 (2000).
[19] G. M. Harry, J. Houser, and K. A. Strain, Phys. Rev. D **65**, 082001 (2002).
[20] P. Falferi, M. Bonaldi, M. Cerdonio, A. Vinante, R. Mezzena, and G. A. Prodi, and S. Vitale, Appl. Phys. Lett. **88**, 062505 (2006).
[21] L. Gottardi, Ph.D. thesis, Leiden University, Leiden, The Netherlands, 2004.
[22] A. Vinante, M. Bonaldi, P. Falferi, M. Cerdonio, R. Mezzena, G. Prodi, and S. Vitale, in Proceedings of the SQUID 2001 Conference, 2001 (unpublished); Stenungsbaden and Sweden, Physica C (Amsterdam) **368**, 176 (2002).
[23] L. Baggio, M. Cerdonio, A. Ortolan, G. Vedovato, L. Taffarello, J. P. Zendri, M. Bonaldi, P. Falferi, V. Martinucci, and R. Mezzena, *et al.*, Phys. Rev. D **61**, 102001 (2000).
[24] C. W. Misner, K. S. Thorne, and J. Wheeler, *Gravitation* (Freeman, San Francisco, 1973).
[25] P. Astone, D. Babusci, M. Bassan, P. Carelli, G. Cavallari, E. Coccia, C. Cosmelli, S. D'Antonio, V. Fafone, and A. Fauth, *et al.*, Phys. Rev. Lett. **91**, 111101 (2003).
[26] S. M. Merkowitz and W. W. Johnson, Phys. Rev. D **56**, 7513 (1997).
[27] K. Yamamoto, S. Otsuka, Masaki, K. Kawabe, and K. Tsubono, Classical Quantum Gravity **19**, 1689 (2002).
[28] W. W. Johnson and S. M. Merkowitz, Phys. Rev. Lett. **70**, 2367 (1993).
[29] C. W. Helstrom, *Statistical Theory of Signal Detection* (Pergamon, Oxford, 1968).
[30] F. Dubath, J. Extermann, and L. Gottardi (unpublished).
[31] P. Saulson, Phys. Rev. D **42**, 2437 (1990).
[32] E. Majorana and Y. Ogawa, Phys. Lett. A **233**, 162 (1997).
[33] A. de Waard, Y. Benzaim, G. Frossati, L. Gottardi, H. van der Mark, J. Flokstra, M. Podt, M. Bassan, Y. Minenkov, and A. Moleti, *et al.*, Classical Quantum Gravity **22**, S215 (2005).
[34] Y. Levin, Phys. Rev. D **57**, 659 (1998).
[35] T. Briant, M. Cerdonio, L. Conti, A. Heidmann, A. Lobo, and M. Pinard, Phys. Rev. D **67**, 102005 (2003).
[36] P. Falferi, M. Cerdonio, L. Franceschini, R. Macchietto, S. Vitale, and J. P. Zendri, Rev. Sci. Instrum. **65**, 2916 (1994).
[37] P. Falferi, M. Bonaldi, A. Cavalleri, M. Cerdonio, A. Vinante, R. Mezzena, K. Xu, G. A. Prodi, and S. Vitale, Appl. Phys. Lett. **82**, 931 (2003).
[38] C. M. Caves, Phys. Rev. D **26**, 1817 (1982).
[39] H. L. V. Trees, *Detection, Estimation, and Modulation Theory. Part I* (John Wiley & Sons, New York, 1968).
[40] To obtain large capacitance one could, for example, make use of a double electrode scheme as proposed in [42]. However, transducers with such a large mass and capacitance and high Q have never been developed so far and the feasibility needs to be demonstrated.
[41] N. Solomonson, W. W. Johnson, and W. O. Hamilton, Phys. Rev. D **46**, 2299 (1992).
[42] M. Bassan, Y. Minenkov, and G. Zaccarian, in *Proceedings of the 1st Edoardo Amaldi Conf. on Gravitational Waves* (World Scientific, Singapore, 1995), p. 358.
[43] A. de Waard, L. Gottardi, M. Bassan, E. Coccia, V. Fafone, J. Flokstra, A. Karbalai-Sadegh, Y. Minenkov, A. Moleti, and G. V. Pallottino, *et al.*, Classical Quantum Gravity **21**, S465 (2004).
[44] R. P. Giffard, Phys. Rev. D **14**, 2478 (1976).
[45] S. M. Merkowitz, J. A. Lobo, and M. A. Serrano, Classical Quantum Gravity **16**, 3035 (1999).
[46] N. Arnaud, M. Barsuglia, M.-A. Bizouard, P. Canitrot, F. Cavalier, M. Davier, P. Hello, and T. Pradier, Phys. Rev. D **65**, 042004 (2002).